processes

MDPI

*Article*

# Interaction Mechanism of Inter-Pipes in Double-Layer Pipelines and a Mechanical Model with Differential Thermal Deformation

**Gang Qiu [1,*] and Mingming Sun [2,3,4,5]**

[1] Architectural Engineering Institute, Xinyang Vocational and Technical College, Xinyang 464000, China
[2] School of Water Resources and Transportation, Zhengzhou University, Zhengzhou 450001, China; mingmingsunyan@163.com
[3] State Key Laboratory of Tunnel Boring Machine and Intelligent Operations, Zhengzhou 450001, China
[4] National Local Joint Engineering Laboratory of Major Infrastructure Testing and Rehabilitation Technology, Zhengzhou 450001, China
[5] Collaborative Innovation Center of Water Conservancy and Transportation Infrastructure Safety, Zhengzhou 450001, China
* Correspondence: qiugang@xyvtc.edu.cn

**Abstract:** Double-layer pipelines are widely used in deep-sea energy transport because of their strong thermal insulation and enhanced structural safety. The stress distribution and the interaction mechanism between inter-pipes of double-layer pipelines are elucidated. A mechanical model is developed to characterize the thermal deformation difference between the two layers. The mechanical response of the pipeline can be divided into two distinct modes based on the initial deformation stages: (1) an inner-pipe-dominated elongation that creates compressive stress in the inner pipe and tensile stress in the outer pipe, and (2) an outer-pipe-dominated elongation that reverses this stress distribution. Sagging deformation (bowl-shaped deformation), primarily caused by the self-weight of the inner pipe, is identified as the critical factor that drives the stress concentration and bending moment at the inner–outer pipe connection. Engineering approaches, such as inserting spacers or additional supports in the annular cavity, effectively reduce peak stresses in both layers under extreme conditions.

**Keywords:** double-layer pipeline; mechanical modeling; pipe interaction; sagging deformation; spring element

check for updates

Academic Editor: Chin-Hyung Lee

Received: 6 February 2025
Revised: 1 March 2025
Accepted: 3 March 2025
Published: 6 March 2025

**Citation:** Qiu, G.; Sun, M. Interaction Mechanism of Inter-Pipes in Double-Layer Pipelines and a Mechanical Model with Differential Thermal Deformation. *Processes* **2025**, *13*, 762. https://doi.org/10.3390/pr13030762

**Copyright:** © 2025 by the authors. Licensee MDPI, Basel, Switzerland. This article is an open access article distributed under the terms and conditions of the Creative Commons Attribution (CC BY) license (https://creativecommons.org/licenses/by/4.0/).

## 1. Introduction

The exploitation of marine resources has been ongoing for more than seventy years, gradually depleting shallow-water reserves [1]. Since the 1980s, exploration efforts have shifted toward deep-water regions, leading to the development of major oil fields in Brazil, the North Sea, and the Gulf of Mexico [2,3]. In offshore applications, pipe-in-pipe (PIP) systems commonly consist of an outer pressure-resistant protective pipe to isolate seawater and an inner conduit for oil and gas transport. Two main PIP configurations exist: fully filled and partially filled [4].

Fully filled PIP systems employ rigid concentric pipes with their annular space fully or predominantly occupied by polyurethane foam, mineral wool, aerogel, or ceramics. In contrast, partially filled systems incorporate centralizers on the inner pipe for stabilization, allowing sliding within the outer pipe while optionally filling portions of the annulus with insulation or working fluids. Fully filled systems excel in thermal insulation and structural stability, making them well-suited for harsh environments or high-strength requirements. Partially filled systems offer greater flexibility and cost savings, especially

where thermal expansion or simpler installation is vital. Selection depends on thermal insulation requirements, pipeline movement, the environment, cost, and maintenance.

In deep-sea oil transportation, where crude oil pour points often exceed seabed temperatures, thermal insulation is critical to prevent solidification. Hence, fully filled PIP systems with intermediate insulation layers are often the standard solution [5,6]. Table 1 presents the main application areas of double-layered pipelines. As illustrated in Figure 1, the double-layer steel pipeline comprises concentric inter-pipes separated by an insulating medium, offering the following advantages:

(1) The outer pipe mechanically protects the insulation layer and partially resists extreme seabed loads.
(2) It serves as a ballast to prevent pipeline buoyancy.
(3) The dual-pipe configuration increases cross-sectional area, enhancing load-bearing capacity.
(4) The insulation layer maintains optimal temperature conditions for the transported medium.
(5) The outer pipe contains potential leaks, mitigating marine environmental risks.

**Table 1.** Engineering applications of double-layer pipelines.

| Length/km | Location | Water Depth/m | Dimension/mm | Insulation Material | Completion Year |
|---|---|---|---|---|---|
| 25 | Congo | 200 | 254/304.8 | IZOFLEX(granules) | 2000 |
| 16.1 | Gulf of Mexico | 1341 | 304.8/203.2 | - | 2001 |
| 13.2 | Gulf of Mexico | 1036 | 254/152.4 | - | 2001 |
| 35.4 | Gulf of Mexico | 882 | 254/152.4 | - | 2003 |
| 16.8 | Gulf of Mexico | 882 | 304.8/203.2 | - | 2004 |
| 25 | France | 15 | 609/863.6 | IZOFLEX | 2004 |
| 8 | Peru | 1100 | 406.4/609 | IZOFLEX | 2004 |
| 37 | Nigeria | 140 | 254/304.8 | IZOFLEX | 2005 |
| 33 | UK North Sea | 1470 | 381/431.1 | IZOFLEX | 2005 |
| 66 | West Africa | 170 | 228.6/304.8 | IZOFLEX | 2007 |
| 22 | UK North Sea | 3050 | 406.4/472.4 | IZOFLEX | 2007 |
| 64.4 | Gulf of Mexico | 100 | - | - | 2008 |
| 20 | South China Sea | 2714 | 304.8/508 | PUF (foam) | 2009 |
| 20 | Gulf of Mexico | 2714 | 355.6/228.6 | Aerogel | 2010 |
| 60 | Gulf of Mexico | 200 | 304.8/203.2 | Aerogel | 2010 |

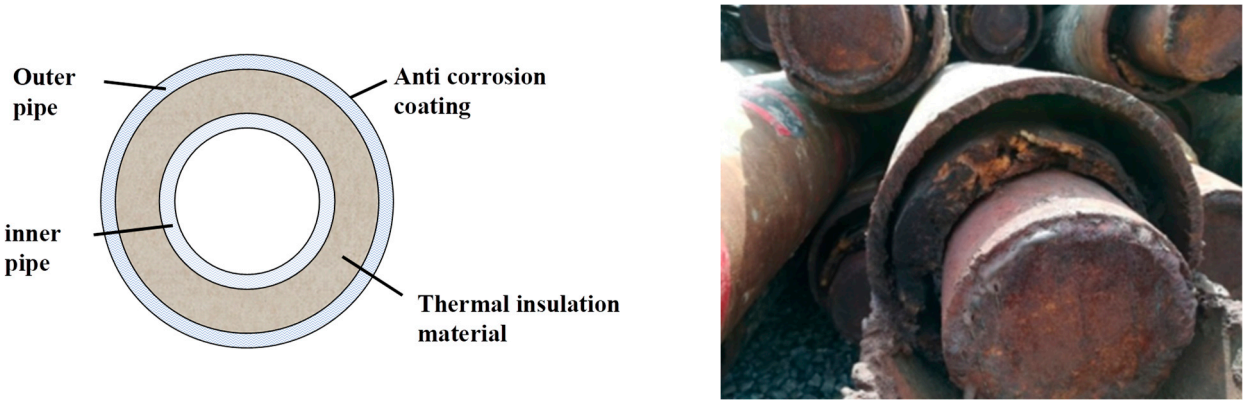



**Figure 1.** Cross-sectional view of the double-layer pipeline (PIP).

Due to the influence of insulation layers and external temperature, the temperature field of double-layered pipelines is non-uniform. The thermal effects of double-layered

pipelines with non-uniform temperature fields differ significantly from those with uniform temperature conditions. The varying thermal conditions experienced by interconnected pipelines result in uncoordinated thermal deformations, which, with the constraints of anchoring components, generate high-stress regions. These stress concentrations impact the structural safety of double-layered pipelines. The fully filled PIP structures, where the annular space is bonded with the inner and outer pipes, can be regarded as either a composite or a sandwich pipe. The load transfer mechanisms between interconnected pipelines lead to structural behaviors that differ considerably from those of single pipes or PIPs with gaps. The axial force distribution also exhibits distinct characteristics.

A rigorous mathematical framework for characterizing thermal expansion behavior in PIP systems was proposed by A. Bokaian [7], who analyzed the displacement and stress of the connected structure. M.A. et al. [8] conducted experimental studies on the thermal energy flow characteristics of sinusoidal smooth inner pipes with varying wavelengths and amplitudes. Guo et al. [9] elucidated the influence mechanism of insulation layers' equivalent stiffness on the stability of PIP systems. T. Sriskandarajah et al. [6] presented anti-buckling and fatigue failure designs for in-service PIP pipelines with high-temperature and high-pressure conditions. J. Acuña and B. Palm [10] performed thermal response experiments on heat exchange conditions between the interconnected pipelines, clarifying the temperature distribution patterns of PIP systems. J. Su and D.R. et al. [5] provided analytical solutions for PIP thermal distribution and simulated the transient heat transfer process during pipeline cooling.

The inner and outer layers of double-layered subsea pipelines are connected through rigid anchoring components or flexible insulation materials. The displacements of the inter-pipes are both mutually constrained and mutually facilitated. Current research on the safety of double-layered pipelines mainly focuses on buckling analysis [11–16] and load-bearing capacity evaluation [17–22] in static problems, as well as vibration control [23–27] and seismic behavior analysis [28] in dynamic problems. However, studies on the thermal response of double-layered pipelines have primarily focused on temperature distribution and the mode of heat transfer between the interconnected pipelines, often neglecting the stress concentration effects at constrained locations caused by differential thermal deformations. To address structural damage resulting from differential deformations, it is essential to clarify the load transfer mechanisms and interaction behaviors between the adjacent pipelines. Therefore, research on the differential thermal deformation of double-layered pipelines is necessary to elucidate the impact mechanisms of non-uniform temperature fields on pipeline structures.

## 2. Finite Element Model of the Pipeline

A three-dimensional nonlinear finite element model was developed based on a representative offshore crude oil pipeline system located in the East China Sea basin. The fully filled PIP system (Figure 1) was chosen to examine how structural components interact under extreme conditions.

### *2.1. Constitutive Model of Pipeline*

The inner and outer pipelines are both 16 Mn, with outer diameters of 168 mm and 273 mm and a wall thickness of 9 mm.

The actual tensile curve from circumferential specimens was adopted as the constitutive model [29–31]. Figure 2 shows a yield strength ($\sigma_y$) of 357 MPa and subsequent strain hardening, leading to a tensile strength ($\sigma_u$) of 507 MPa. Table 2 summarizes these properties and other critical parameters governing the pipeline's structural response.

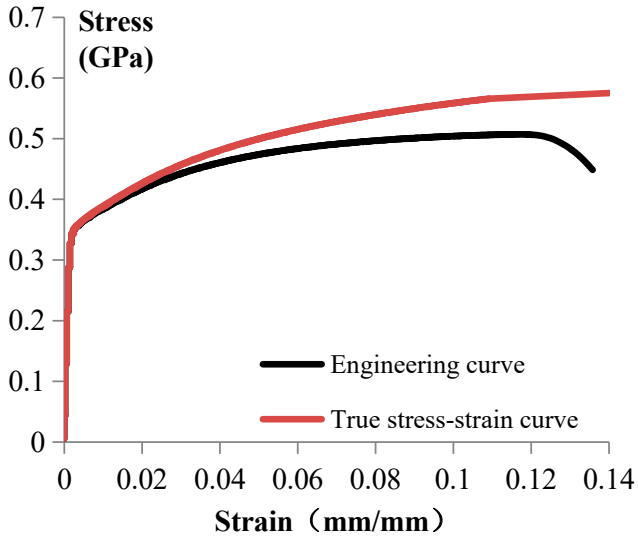


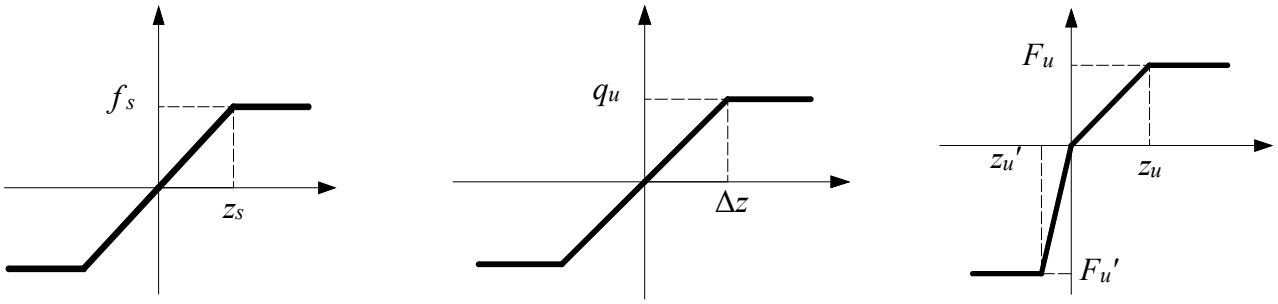

**Figure 2.** Stress–strain curve of 16Mn steel.

**Table 2.** Structural parameters of the subsea pipeline.

| Outer Pipe Diameter (*Φ*) × Wall Thickness (*t*)/mm | Inner Pipe Diameter (*Φ*) × Wall Thickness (*t*)/mm | Elastic Modulus/GPa | Poisson's Ratio | Material |
|---|---|---|---|---|
| 273 × 9 | 168 × 9 | 207 | 0.27 | 16 Mn |

### *2.2. Pipe–Soil Interaction Model*

Ideal elastoplastic pipe–soil spring elements, as specified by the *Guidelines for the Design of Buried Steel Pipe* [32], were employed. Figure 3 illustrates the stiffness curves of soil springs in different directions.




(**a**) Axial direction (horizontal). (**b**) Lateral direction (horizontal). (**c**) Vertical direction.

**Figure 3.** Constitutive model of soil springs.

(1) Axial pipe–soil interaction model (soil friction force)

The yield force of the axial soil spring $f_s$ (N/m) can be determined using Equation (1):

$$f_s = \pi D \alpha_b c_b + \pi D H \overline{\gamma_b} \frac{1 + K_{0b}}{2} \tan \delta_b \quad (1)$$

where $D$ is the diameter; $\overline{\gamma_b}$ is the buoyant unit weight of backfill soil; $c_b$ is the Cohesion of backfill soil; $\alpha_b$ is the adhesion factor, where $\alpha_b = 0.618 - 0.123 c_b - \frac{0.274}{c_b^2+1} + \frac{0.695}{c_b^3+1}$; $H$ refers to the depth of the pipe centerline; $K_{0b}$ is the static lateral pressure coefficient of backfill soil, defined as $K_{0b} \approx 1 - \sin \varphi'$, where $\alpha_b$ is the effective internal friction angle of the backfill soil; and $\alpha_b$ is the friction angle between the pipe and soil, calculated as $\delta_b = \xi \varphi$, where $\alpha_b$

is the internal friction angle and $\xi$ is the friction coefficient of the pipe's surface coating. For steel pipes, $\xi$ typically ranges from 0.5 to 0.7.

The axial elastic limit displacement of the soil spring, $z_s$, is influenced by the type of soil and is presented in Table 3.

**Table 3.** Yield displacement of axial soil springs.

| Soil Type | $z_s$ (mm) | Soil Type | $z_s$ (mm) |
|---|---|---|---|
| Dense sand | 3 | Stiff clay | 8 |
| Loose sand | 5 | Soft clay | 10 |

(2) Horizontal transverse pipe–soil interaction model

The yield force of the horizontal transverse spring per unit length $q_u$ (in N/m) is expressed as follows:

$$q_u = \gamma H N_{qh} D + N_{ch} c D \tag{2}$$

where $\gamma$ is the total unit weight of undisturbed soil, $N_{ch}$ and $N_{qh}$ represent the transverse bending capacity coefficients for cohesive soils and sandy soils, respectively, and $c$ is the cohesion of undisturbed soil.

The horizontal displacement of the soil spring is determined by the following equation:

$$\Delta_z = 0.04(H + \frac{D}{2}) \leq (0.1 \sim 0.15)D \tag{3}$$

(3) Vertical pipe–soil interaction model

① The yield force $F_u$ of the soil spring as the pipe undergoes downward vertical displacement per unit length is shown as follows:

$$F_u = N_c c D + N_q \overline{\gamma} H D + N_r \gamma \frac{D^2}{2} \tag{4}$$

where $N_c$, $N_q$, and $N_r$ denote the bearing capacity coefficients, and $N_q = e^{(\pi \tan \varphi)} \tan^2(45 + \frac{\varphi}{2})$,$N_r = e^{(0.18\varphi - 2.5)}$, and $N_c = [\cot(\varphi + 0.001)]\left\{e^{[\pi \tan(\varphi + 0.001)]} \tan^2(45 + \frac{\varphi + 0.001}{2}) - 1\right\}$. $\overline{\gamma}$ is the buoyant unit weight of undisturbed soil. The yield displacement $z_u$ of the soil spring is provided in Table 4.

**Table 4.** Yield displacement of the downward vertical soil spring.

| Soil Type | $z_u$ |
|---|---|
| Granular soils | 0.1 $D$ |
| Cohesive soils | 0.2 $D$ |

② The yield force of the soil spring when the pipe undergoes upward vertical displacement per unit length is given by the following equation:

$$F_u{}' = N_c{}' c D + N_q{}' \overline{\gamma} H D \tag{5}$$

where $N_c{}'$ is the upward coefficient for cohesive soils. When $c$ = 0, $N_c{}' = 0$; when $c \neq 0$ and $\frac{H}{D} \leq 10$, $N_c{}' = 2\left(\frac{H}{D}\right) \leq 10$. $N_q{}'$ is the vertical upward coefficient of sandy soil. When $\varphi = 0°$, $N_q{}' = 0$; when $\varphi \neq 0°$, $N_q{}' = \left(\frac{\varphi H}{44D}\right) \leq N_q$. The range of values for the yield displacement $z_u{}'$ of the spring is shown in Table 5.

**Table 5.** Yield displacement of the upward vertical soil spring.

| Soil Type | $z_u'$ |
|---|---|
| Sandy soils | 0.01 $H$~0.02 $H$ (<0.1 $D$) |
| Cohesive soils | 0.1 $H$~0.2 $H$ (<0.2 $D$) |

### 2.3. Spring Units for Inner and Outer Pipes

A gap of approximately 0.02 m separates the insulation layer from the inner wall of the outer pipe, with an inter-pipe distance of 0.0435 m. Special spring elements (Figure 4) simulate the contact interactions.

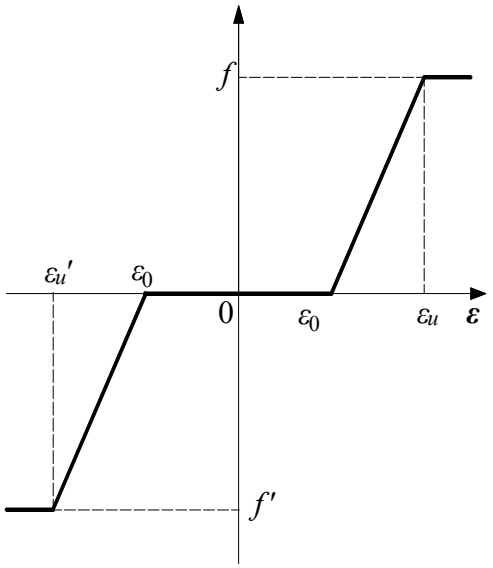



**Figure 4.** Spring element model of inner and outer tubes.

① As the inner pipe displacement is within [0, δ], it remains free to move within the gap, and the spring element remains unforced.

② As the displacement exceeds $\varepsilon_0$, the insulation contacts the outer pipe's inner wall, initiating load transfer between the inter-pipes. The constitutive model of the contact spring between the inter-pipes indicates that the spring force increases as the displacement grows.

③ As $\varepsilon = \varepsilon_u$, the spring yields and the inter-pipes essentially form an integrated system. At the point where the connection spring element yields, the soil spring element of the outer pipe also yields. The yielding force is determined by the properties of the soil spring. For horizontal transverse springs, the yielding force is defined as $f = f' = q_u$ and $\varepsilon_u = \varepsilon_u' = \Delta_z + 0.0435$. In the vertical direction, as the pipe undergoes downward vertical displacement per unit length, the yielding force of the double-pipe spring element is $f = F_u$ and $\varepsilon_u = z_u + 0.0435$; as the pipe undergoes upward vertical displacement per unit length, the yielding force of the double-pipe spring element is $f' = F_u'$ and $\varepsilon_u' = z_u' + 0.0435$.

The spring elements connecting the inter-pipes are only present in the horizontal and vertical directions. The axial constraint of the inner pipe is achieved through the forgings that link the inter-pipes. The spring element nodes in the horizontal and vertical directions are coupled with the degrees of freedom of the corresponding nodes on the outer pipe with the "*cp*" command in ANSYS 17.0, as illustrated in Figure 5.

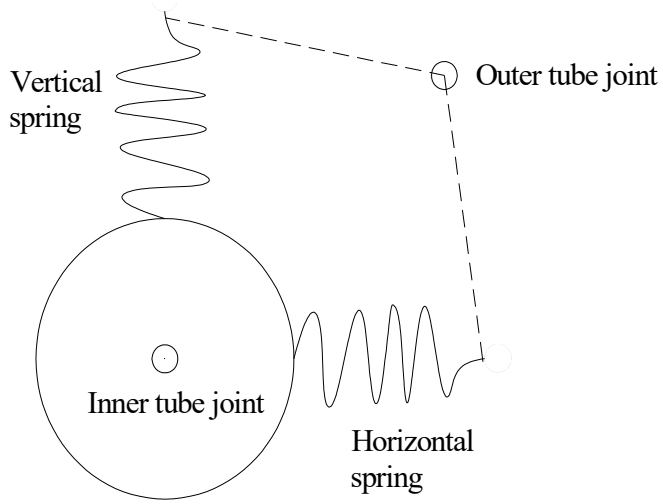



**Figure 5.** Connection method of spring elements between inter-pipes.

### *2.4. Finite Element Model*

The inner and outer pipes connect at both ends via forgings (with a length of 0.25 m), creating a 500 m annular cavity designed to contain leaks. The forgings are illustrated in Figures 6 and 7. As the pipeline is in the laying stage, internal pressure is neglected to focus on thermal and gravitational effects.

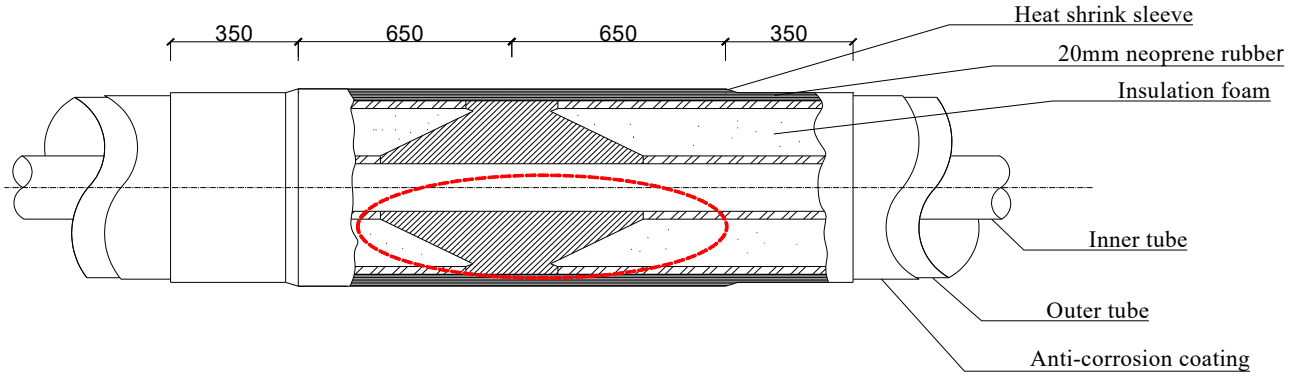



**Figure 6.** Typical rigid joint connection diagram.

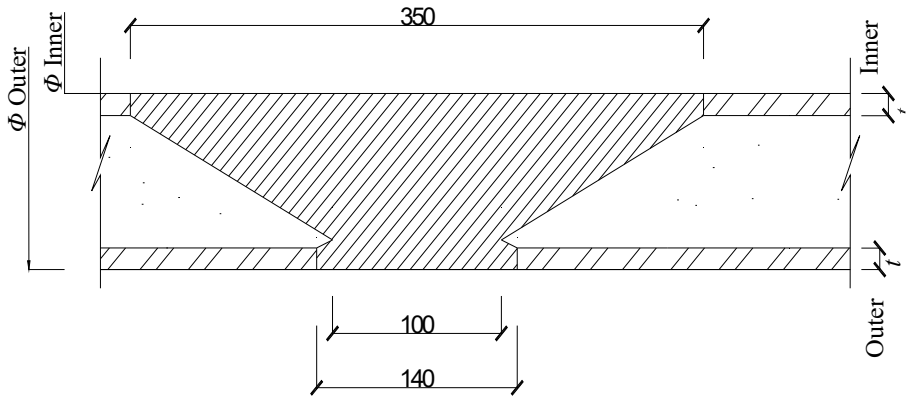



**Figure 7.** Rigid joint connection.

The dual-layer pipe system was simulated with the Pipe20 element in ANSYS 17.0. A finite element model of a 500 m dual-layer pipe system was established. The nodes at both ends of the inter-pipes within a 0.25 m range were coupled, and spring elements were applied to connect the intermediate nodes of the inner and outer pipes. Figure 8 illustrates

the finite element constraints and coupling model. Tables 6 and 7 summarize the soil and environmental parameters, respectively.

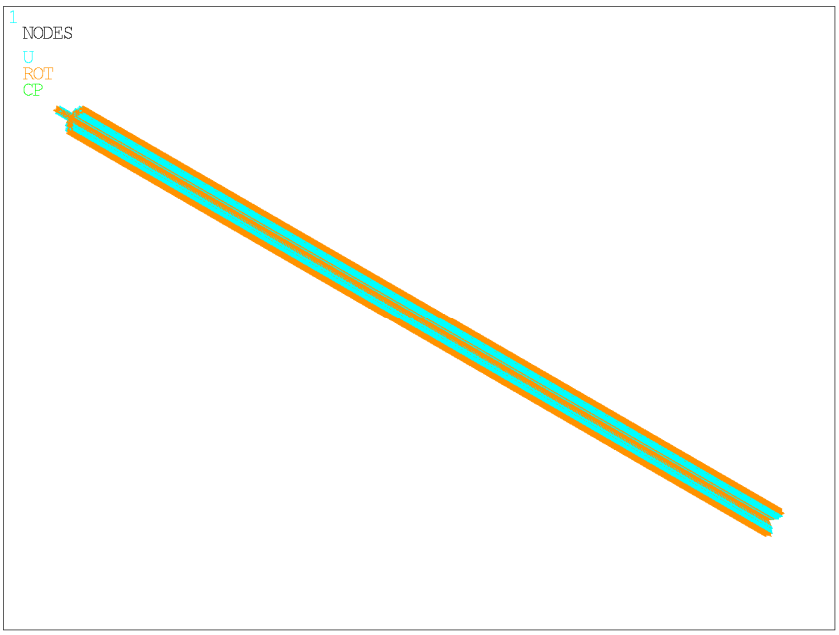



**Figure 8.** Constraints and coupling model of PIP.

**Table 6.** Soil parameters.

| Cohesion (kPa) | Effective Unit Weight (N/m) | Internal Friction Angle (°) | Total Unit Weight (N/m) | Friction Coefficient |
|---|---|---|---|---|
| 30 | 16,700 | 20 | 19,700 | 0.7 |

**Table 7.** Environmental parameters.

| Crude Oil Density (kg/m$^3$) | Steel Density (kg/m$^3$) | Burial Depth (m) | Water Depth (m) | Pipeline Length (m) |
|---|---|---|---|---|
| 860 | 7850 | 1.5 | 2.3 | 500 |

The plastic mechanical behavior of the polyurethane foam was described with the crushable isotropic hardening foam model developed by Deshpande et al. [33]. The density of the polyurethane foam is 110 kg/m$^3$, and its stress–strain behavior was modeled based on the experimental data obtained by Wang et al. [34]. The polyurethane foam material parameters based on the crushable foam model are shown in Table 8.

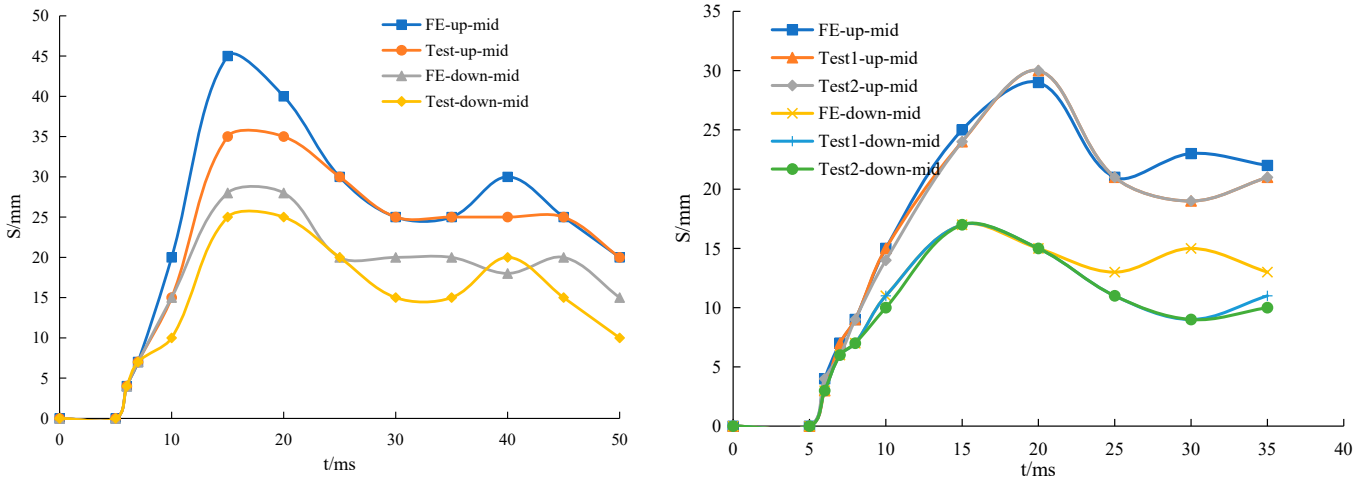
**Table 8.** Material parameters of the crushable foam model of polyurethane foam.

| Density $\rho$ (kg·m$^{-3}$) | Yield Stress (MPa) | Elastic Modulus (MPa) | Elastic Poisson's Ratio | Yield Stress Ratio | Plastic Poisson's Ratio |
|---|---|---|---|---|---|
| 100 | 0.7 | 16 | 0.3 | 1 | 0 |

### *2.5. Finite Element Model Validation*

To validate both the FE model and the inter-pipe interaction, lateral load failure tests conducted by Gao et al. [35] were adopted. As the main focus is on the mechanical response of a double-layer pipeline system with temperature deformation, the midspan deformation of the outer pipe in the failure experiment is used as the verification parameter. Figure 9

shows the comparison between experimental results and numerical results. It can be seen that the trend and the numerical values of numerical and experimental results are basically consistent. Table 9 provides a comparison of key parameters, and it can be seen from the table that the lateral deformation error is the largest among the key parameters, at around 5%. The error of the remaining parameters is not higher than 2.1%, which meets the error requirements of the FE model and verifies the accuracy of the model.




(**a**) PFG. (**b**) PHA.

**Figure 9.** Comparison of experimental and numerical results.

**Table 9.** Comparative analysis of key parameters.

| Test Condition | PFG | | PHA | |
|---|---|---|---|---|
| | Numerical Result | Error | Numerical Result | Error |
| Maximum load | 1380 kN | 2% | 1331 kN | 1.5% |
| Lateral deformation | 45 mm | 5.2% | 30.2 mm | 4.6% |
| Maximum diameter of outer tube | 296.7 mm | 2.1% | 349.8 mm | 0.98% |

Note: Error = (experimental result − numerical result)/experimental result × 100%.

## 3. Extreme Operating Conditions

Two major extreme operating conditions arise from environmental variations and transported fluid temperatures, leading to differential pipeline deformation:

### *3.1. Ambient Temperature*

The pipeline was designed between April and May 1994, and construction occurred between October and December 1994. The annual average air temperature in the region was 11.7 °C, with monthly temperature variations listed in Table 10.

**Table 10.** Monthly air temperature variations (February 1985–December 1989, °C).

| Month | 1.0 | 2.0 | 3.0 | 4.0 | 5.0 | 6.0 | 7.0 | 8.0 | 9.0 | 10.0 | 11.0 | 12.0 | Year |
|---|---|---|---|---|---|---|---|---|---|---|---|---|---|
| Maximum | 9.5 | 14.1 | 19.6 | 31.2 | 36.3 | 39.6 | 36.6 | 35.3 | 34.5 | 30.3 | 21.8 | 18.6 | 39.6 |
| Average | −3.5 | −2.2 | 3.2 | 11.8 | 18.9 | 22.1 | 24.9 | 25.9 | 20.8 | 14.3 | 5.3 | −1.7 | 11.7 |
| Minimum | −16.6 | −12.7 | −8.0 | −2.0 | 5.0 | 11.5 | 17.3 | 16.4 | 10.1 | −2.6 | −8.2 | −18.0 | −18.0 |

Based on the observations from the Yellow River Harbor Ocean Station in 2008, the annual average seawater temperature was 13.6 °C, with a maximum of 29.6 °C and a minimum of −5.2 °C. Table 11 shows the monthly seawater temperature. Except for

January and February, the monthly average seawater temperature exceeded 0 °C, with temperatures from June to September exceeding 20 °C. During winter (December, January, and February), temperatures fell below 0 °C, while the minimum seawater temperature during other seasons remained above 0 °C.

**Table 11.** Monthly seawater temperature variations (January 2008–December 2008, °C).

| Month | 1 | 2 | 3 | 4 | 5 | 6 | 7 | 8 | 9 | 10 | 11 | 12 | Year |
|---|---|---|---|---|---|---|---|---|---|---|---|---|---|
| Maximum | 0.6 | 5.9 | 11.1 | 17.2 | 22.4 | 24.8 | 28.1 | 29.6 | 26.6 | 21.0 | 13.9 | 7.2 | 29.6 |
| Average | −0.6 | −0.2 | 6.4 | 12.1 | 17.8 | 21.5 | 25.0 | 26.9 | 24.0 | 17.3 | 10.2 | 1.5 | 13.6 |
| Minimum | −3.5 | −5.2 | 2.1 | 9.1 | 14.8 | 18.3 | 22.0 | 24.7 | 16.0 | 10.8 | 2.2 | −5.0 | −5.2 |

### *3.2. Extreme Condition*

(1) Extreme Condition 1: Outer Pipe Shrinkage (Cooling)

During pipeline installation, the ambient temperature may be higher than the seabed water temperature. The outer pipe undergoes contraction due to thermal stress as a result of pre-cooling, while the inner pipe remains unaffected due to the insulation layer. As the inner pipe is connected to the outer pipe, it experiences deformation caused by the bending moment induced by the deformation of the outer pipe at both ends.

To analyze the extreme conditions for the shrinkage of the outer tube, December is identified as the month with the greatest temperature difference. The ambient temperature is taken as 18.6 °C (the maximum temperature of December in Table 10), and the seawater temperature is taken as −5 °C (the minimum temperature of December in Table 11), resulting in a temperature difference of −23.6 °C.

(2) Extreme Condition 2: Outer Pipe Expansion (Heating)

During the pipeline installation process, as the ambient temperature is lower than the seabed water temperature, the outer pipe undergoes thermal expansion with the influence of thermal stress. In contrast, the inner pipe remains thermally unaffected due to the insulation layer.

In this operational scenario, the minimum ambient temperature of −18 °C (the minimum temperature of December in Table 10) and the maximum seawater temperature of 7.2 °C (the maximum temperature of December in Table 11) recorded during December collectively establish a thermal differential of 25.2 °C across the pipeline system.

## 4. Analysis of Extreme Conditions

### *4.1. Verification of Results*

A key calculation is the inner pipe constraint: its displacement must be greater than zero but less than 0.0435 m. The soil parameters in Table 6 were used to calculate the pipe–soil interaction model. Table 12 presents the verification of the inner pipe displacement for two extreme conditions. The results indicate that the lateral deformation of the inner pipe is negligible without lateral forces. The maximum relative displacement of the inner pipe is calculated to be 0.020536 m, exceeding the clearance gap of 0.02 m. After the insulation material comes into contact with the inner wall of the outer pipe, the deformation becomes minimal due to the constraint provided by the surrounding soil, resulting in a deformation of only 0.536 mm. These findings demonstrate that the double-layer pipeline model aligns with real-world conditions.

**Table 12.** Verification of inner pipe displacement.

| Direction | Horizontal (m) | | Vertical (m) | |
|---|---|---|---|---|
| Extreme Condition 1 | Maximum absolute displacement | 0 | Maximum absolute displacement | 0.00003597 |
| | Minimum absolute displacement | 0 | Minimum absolute displacement | −0.0205 |
| | Maximum relative displacement | 0 | Maximum relative displacement | 0.020536 |
| Extreme Condition 2 | Maximum absolute displacement | 0 | Maximum absolute displacement | 0.000036 |
| | Minimum absolute displacement | 0 | Minimum absolute displacement | −0.0205 |
| | Maximum relative displacement | 0 | Maximum relative displacement | 0.020536 |

### *4.2. Results of Extreme Condition 1*

#### 4.2.1. Equivalent Stress Analysis of Inner and Outer Pipes

Figure 10 illustrates the outer pipe's equivalent stress. With pre-cooling, it contracts axially, constrained by the soil. Most segments have stresses from 20.6 to 23.8 MPa. Extreme stresses occur at the pipe ends due to the reaction forces from the inner pipe. The maximum equivalent stress of 36.6 MPa is observed in the "−y" direction (lower end of the pipe), while the minimum equivalent stress of 7.69 MPa is observed in the "+y" direction (upper end of the pipe). The safety factor FS is defined as the ratio of the yield stress of the pipeline to the extremum stress $\sigma_{apply}$: FS = $\sigma_y/\sigma_{apply}$. The calculated safety factor (FS = 9.75) exceeds the minimum requirement ($FS_{min}$ = 1.5).

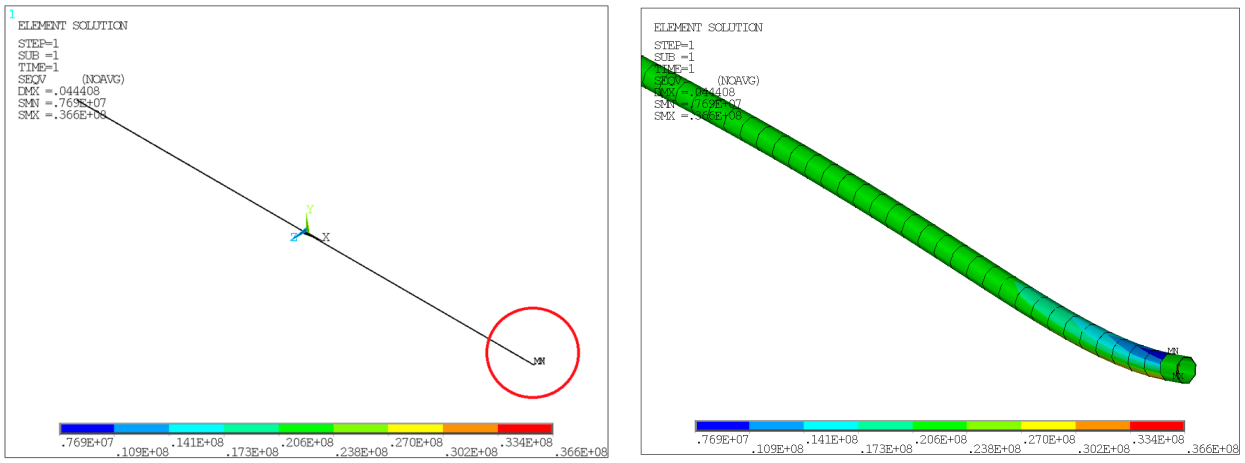



**Figure 10.** Equivalent stress of outer pipe with Extreme Condition 1. (Note: "DMX=.04408" means "Displacement Max = 0.04408 mm"; "SMN=.769E+07"means "Stress Min = 0.769 × $10^7$ Pa"; "SMX=.366E+08"means "Stress Max = 0.366 × $10^8$ Pa and the same notation applies throughout.)

Figure 11 presents the equivalent stress distribution of the inner pipe. Contraction of the outer pipe due to cooling causes the inner pipe ends, which are connected to the outer pipe via forgings, to move toward the center. Although the inner pipe tends to form a "bow" shape, the constraint imposed by the outer pipe wall prevents relative deformation of the middle part of inner tube. Consequently, the remaining sections of the inner pipe reach the clearance displacement, forming a basin-like shape, as shown in the figure.

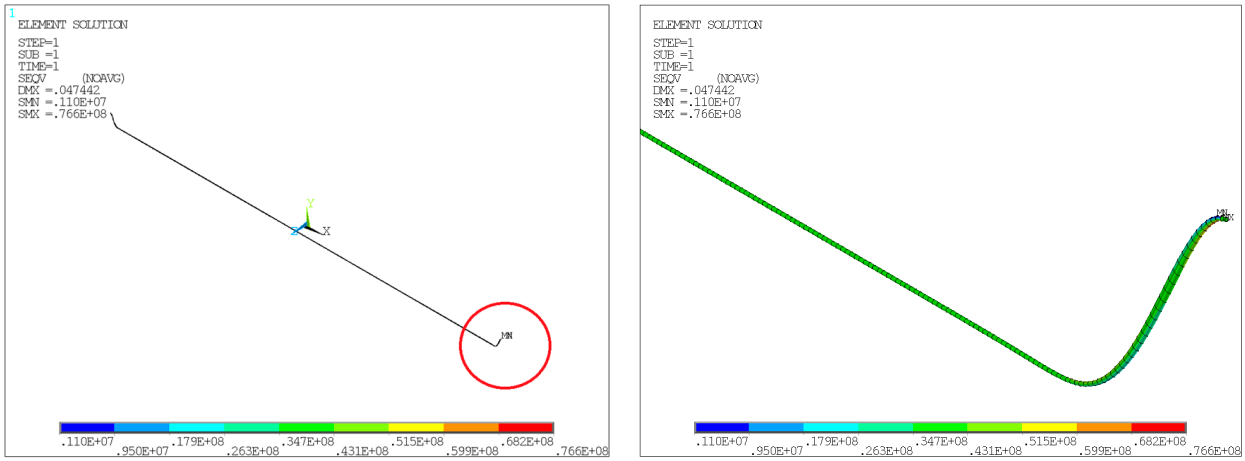



**Figure 11.** Equivalent stress of inner pipe with Extreme Condition 1.

Outer pipe contraction restrains the inner pipe's vertical deformation, creating compressive stress in the inner pipe. Excluding the ends, inner pipe stresses range from 34.7 to 43.1 MPa. At the pipe ends, the maximum equivalent stress of 76.6 MPa occurs in the "−y" direction (lower end of the pipe), while the minimum equivalent stress of 1.1 MPa is observed in the "+y" direction (upper end of the pipe). The calculated safety factor (FS = 4.66) exceeds the minimum requirement ($FS_{min}$ = 1.5).

#### 4.2.2. Axial and Hoop Stress of the Outer Pipe

Considering that the pipe primarily bears axial and hoop stresses, the axial and hoop stresses at 0°, 90°, 180°, and 270° orientations were extracted with different operating conditions for analysis. Figures 12–15 illustrate the distribution of axial stresses along the outer pipe at four orientations. The outer pipe experiences tensile stress due to thermal contraction when cooled, constrained by the surrounding soil. The axial stress distributions at 90° and 270° orientations remain constant with 22.2 MPa. In contrast, the axial stress distributions at 0° and 180° orientations vary along the pipe. Near the pipe ends, the stress at 0° and 180° orientations changes due to the reaction forces from the inner pipe. The outer pipe experiences tensile stress under cooling-induced contraction, with an average axial stress of 22.2 MPa in the midsections.

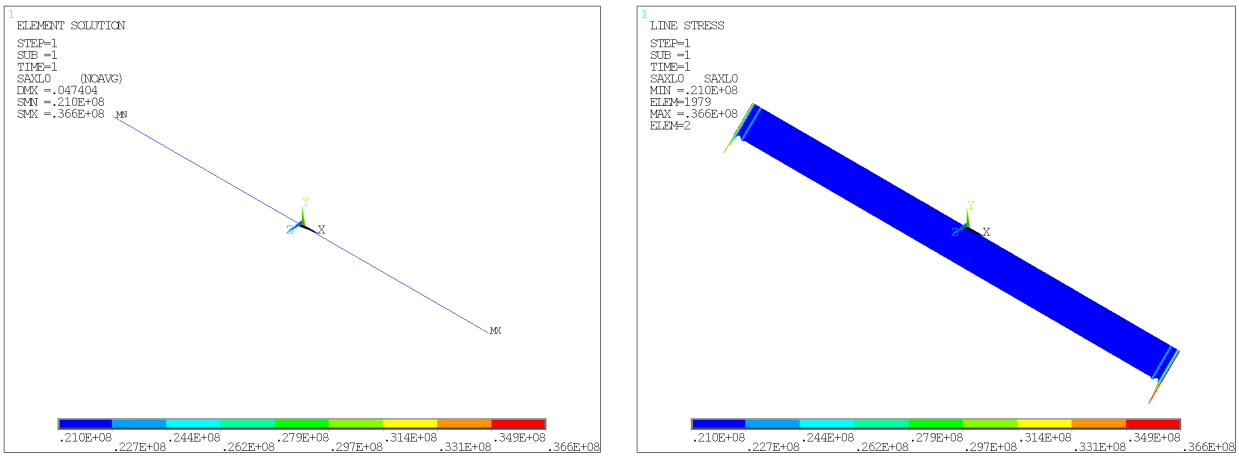



**Figure 12.** Axial stress at 0° orientation with Extreme Condition 1.

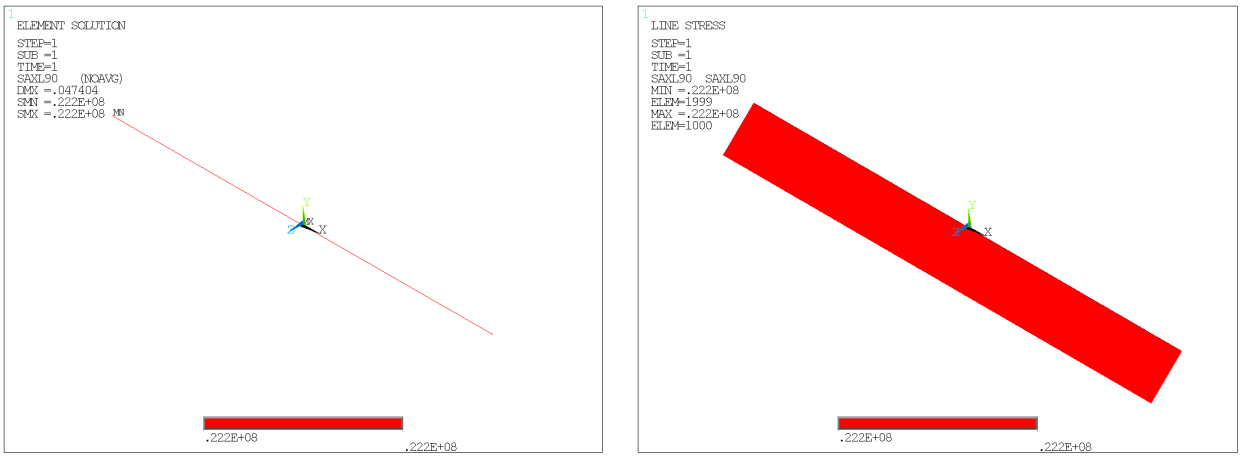



**Figure 13.** Axial stress at 90° orientation with Extreme Condition 1.

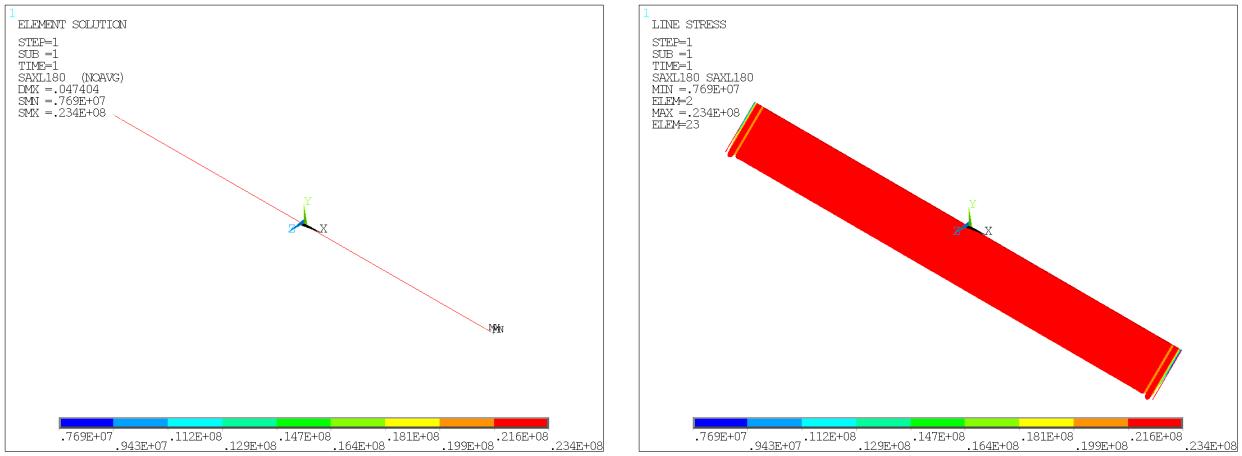



**Figure 14.** Axial stress at 180° orientation with Extreme Condition 1.

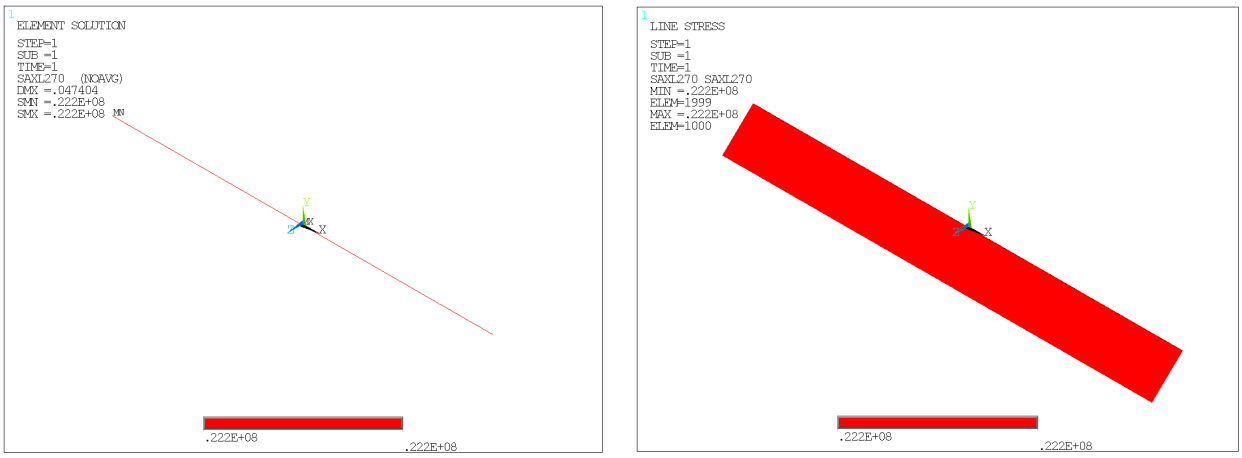



**Figure 15.** Axial stress at 270° orientation with Extreme Condition 1.

Figure 16 shows the bending moment at both ends of the pipe. Due to thermal contraction of the outer pipe, tensile stress is generated. Due to the rigid connection between the inter-pipes at both ends, the inner pipe undergoes axial shortening deformation on the basis of the deformation of the outer pipe. After the inner pipe is compressed, a reaction force directed toward the end of the pipe section is generated on the outer pipe. The elevation difference between the inter-pipes generates a negative bending moment ($-M$) at

the outer pipe extremities through reactive force transmission. This moment redistribution induces a characteristic stress dichotomy: tensile stresses in the negative y-axis orientation (180°) diminish to a minimum of 7.69 MPa, while concurrently, positive y-axis tensile stresses (0°) escalate to a peak magnitude of 36.6 MPa.

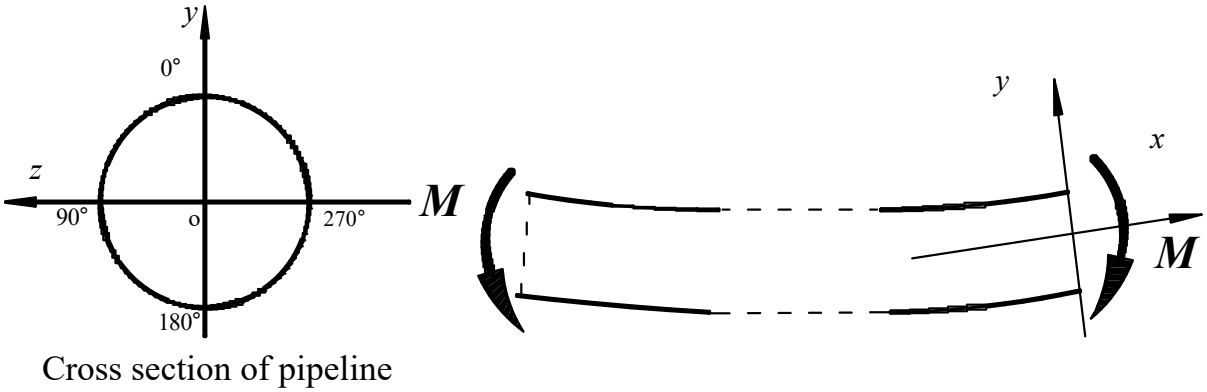



**Figure 16.** Bending moment of Extreme Condition 1.

Table 13 compares the stress at different orientations of the outer pipe. The hoop stresses are all zero due to the absence of internal pressure. The deformations and stresses of the outer and inner pipes mutually influence and constrain each other. The deformation of the inner pipe induces a negative bending moment ($-\boldsymbol{M}$) at the ends of the outer pipe, reducing the tensile stress at 180° orientation while increasing the tensile stress at 0° orientation. The midspan region of the pipeline exhibited negligible sensitivity to bending moment variations, with the von Mises stress maintaining a stable value of 22.2 MPa throughout the loading sequence. The impact of the bending moment is primarily localized near the pipe ends, with minimal influence on most sections of the pipe. As a result, the average stress value in all four orientations is 22.2 MPa.

**Table 13.** Stress of the outer pipe for Extreme Condition 1.

| Stress Type | Axial Stress | | | | Hoop Stress | | | |
|---|---|---|---|---|---|---|---|---|
| Direction | 0° | 90° | 180° | 270° | 0° | 90° | 180° | 270° |
| Maximum (MPa) | 36.6 | 22.2 | 23.4 | 22.2 | 0 | 0 | 0 | 0 |
| Minimum (MPa) | 21 | 22.2 | 7.69 | 22.2 | 0 | 0 | 0 | 0 |
| Average (MPa) | 22.2 | 22.2 | 22.1 | 22.2 | 0 | 0 | 0 | 0 |

Note: The average stress values represent the mean of all nodal stress values along the pipe.

#### 4.2.3. Axial and Hoop Stresses in the Inner Pipe

Figures 17–20 illustrate the axial stress distribution at four different angular positions. The axial stress distribution at 90° and 270° remains constant along the pipe with a uniform value of 36.7 MPa. However, the axial stress distributions at 0° and 180° vary along the pipe. At the pipe ends in the 0° and 180° directions, the axial stress changes due to the reactive forces exerted by the inner pipe. Excluding the pipe ends, the midsection of the pipe, which is less influenced by direct interaction of the inner pipe, exhibits no variation in stress with 36.7 MPa.

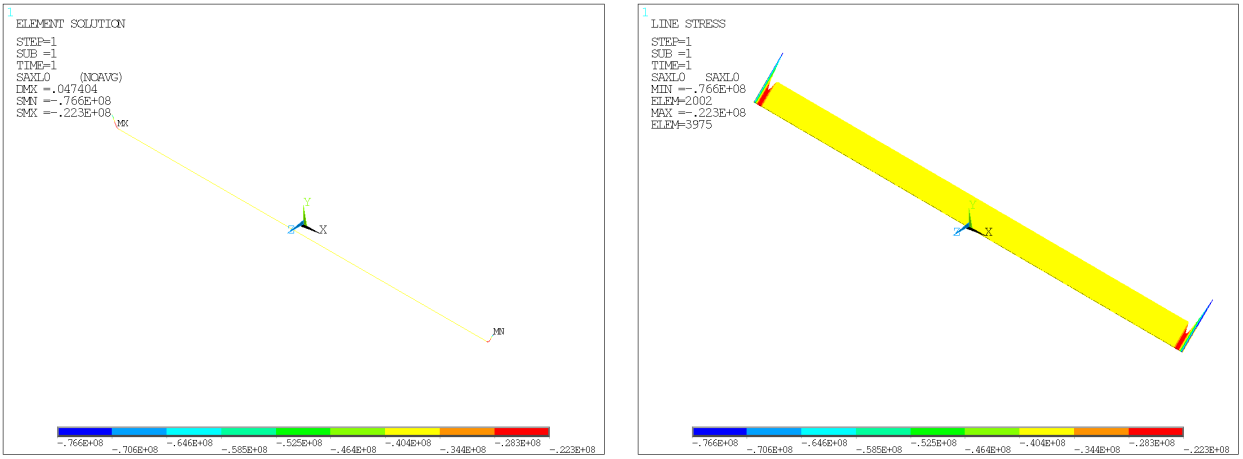



**Figure 17.** Axial stress at 0° for Extreme Condition 1.

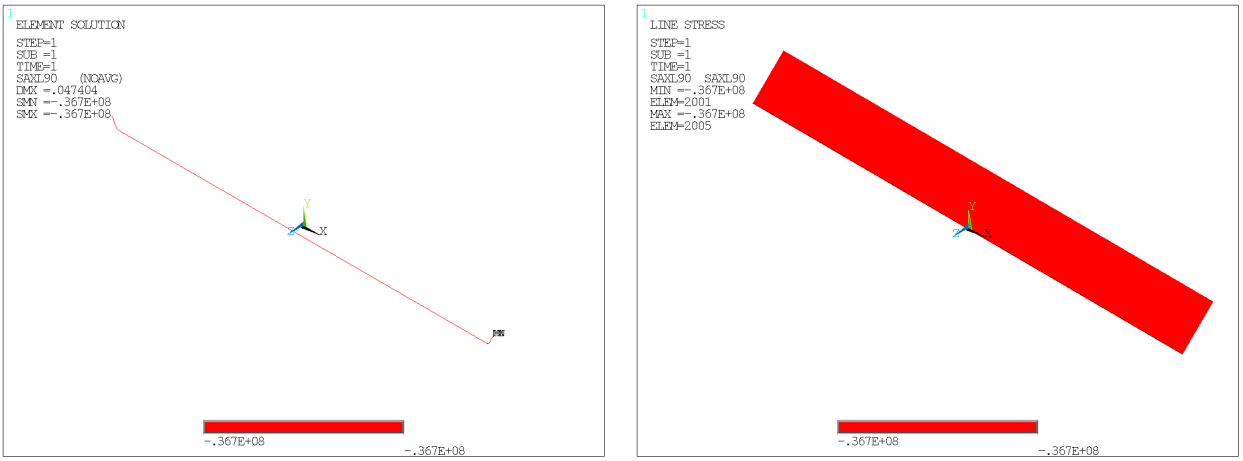



**Figure 18.** Axial stress at 90° for Extreme Condition 1.

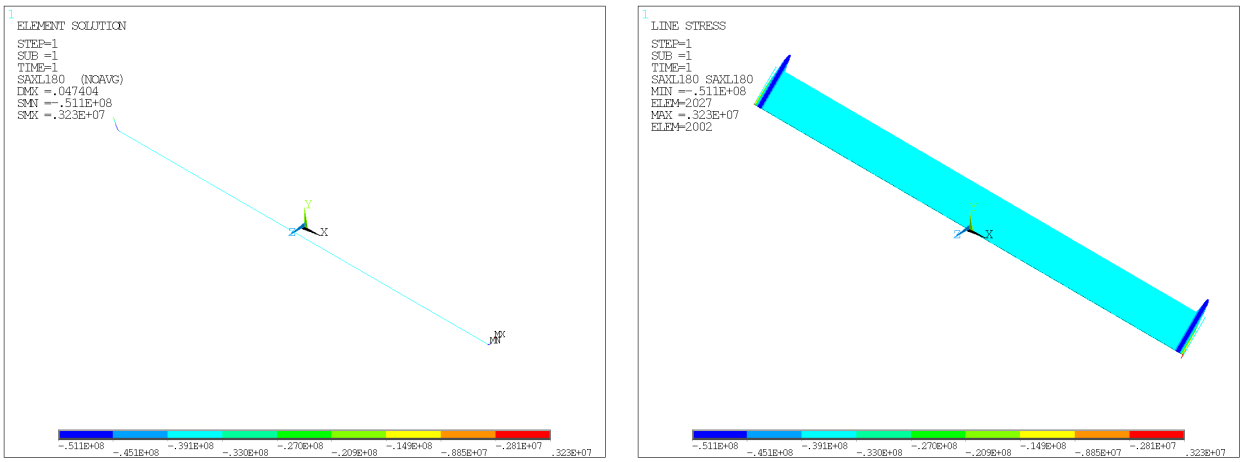



**Figure 19.** Axial stress at 180° for Extreme Condition 1.

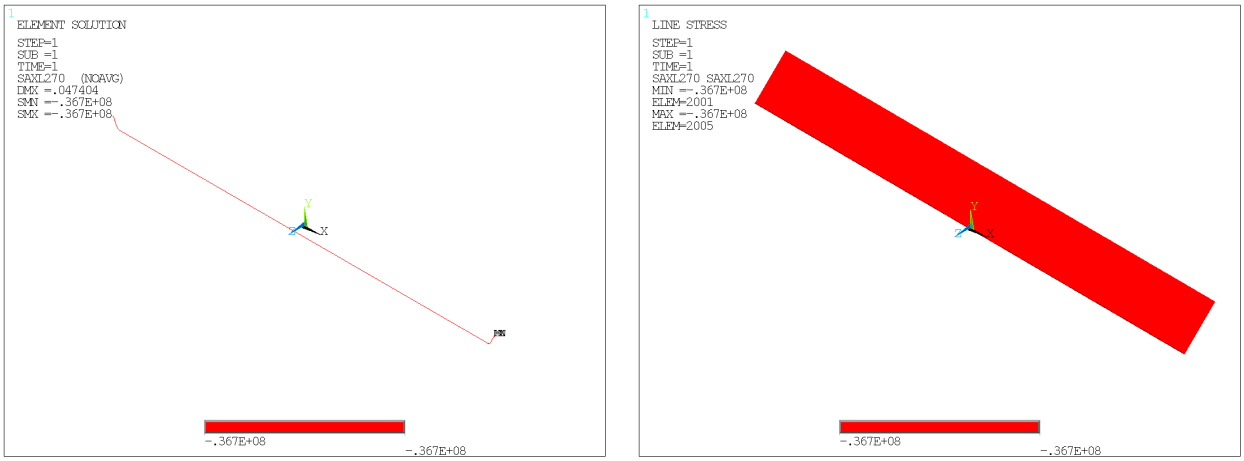



**Figure 20.** Axial stress at 270° for Extreme Condition 1.

Figure 21 depicts the bending moment distribution at both ends of the pipe, indicating that the inner pipe experiences more complex stress conditions compared to the outer pipe. The tensile stress generated in the outer pipe due to pre-cooling shrinkage exerts compressive forces on the inner pipe, as both ends of the inner pipe are rigidly connected to the outer pipe. The connection induces inward displacement of the inner pipe ends, generating compressive stress within the inner pipe.

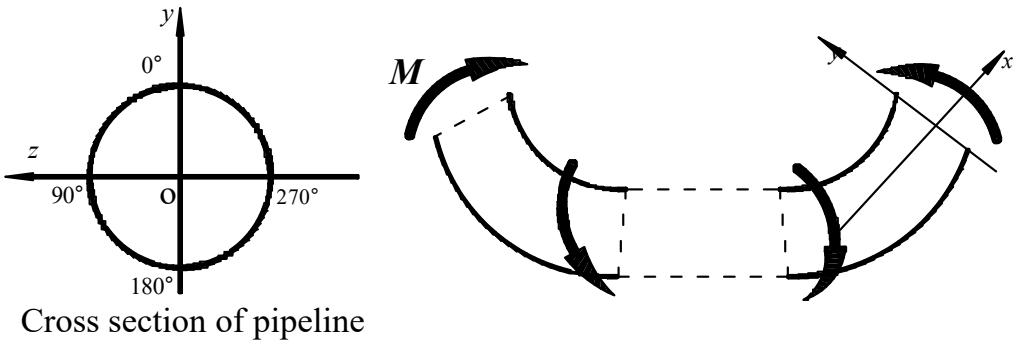



**Figure 21.** Bending moment distribution at the ends of the inner pipe with Extreme Condition 1.

As displacement occurs at the pipe ends, the midsection of the inner pipe remains constrained by the outer pipe walls, maintaining a horizontal alignment. Due to the vertical displacement of the inner pipe under the action of gravity, the elevation of the middle section of the pipeline is lower than that of the end section. The initial deformation resulted in an "***L***"-shaped deformation and a positive bending moment (+***M***) at the end of the inner tube under compressive stress.

The bending moment, coupled with the constraints imposed by the outer pipe walls, causes the vertical segment of the "***L***"-shaped inner pipe at the left end to exhibit a clockwise rotation in the x–y plane. Consequently: ① The compressive stress in the "−y" (180°) direction at the pipe ends decreases, leading to the formation of the only tensile stress element with 3.23 MPa. ② The compressive stress in the "+y" (0°) direction at the pipe ends increases, resulting in a maximum compressive stress of −76.6 MPa.

At the corner of the "***L***"-shaped inner pipe (junction with the horizontal segment): ① The compressive stress in the "−y" (180°) direction increases to −51.1 MPa, exceeding the average stress value of −36.7 MPa. ② The compressive stress in the "+y" (0°) direction decreases to −22.3 MPa, lower than the average stress value of −36.7 MPa. The stress

extremes in the 0° and 180° directions occur at the pipe ends and the "***L***"-shaped corner, respectively.

Table 14 presents a comparison of stress in different directions for Extreme Condition 1. The deformation of the outer pipe affects the inner pipe, inducing "***L***"-shaped deformation at the ends of the inner pipe. The interactions between inter-pipes constrain each other's strain and stress distribution. The deformation of the outer pipe generates a positive bending moment (+***M***) at the ends of the inner pipe, which predominantly impacts the vertical segment of the "***L***"-shaped pipe. The horizontal segment of the "***L***"-shaped pipe and the midsection of the pipe remain largely unaffected, with stress values remaining constant. Due to the localized influence of the bending moment, most segments of the pipe are unaffected, with an average stress value of −36.7 MPa across all directions.

**Table 14.** Stress values in the inner pipe with Extreme Condition 1.

| **Stress Type** | **Axial Stress** | | | | **Hoop Stress** | | | |
|---|---|---|---|---|---|---|---|---|
| Direction | 0° | 90° | 180° | 270° | 0° | 90° | 180° | 270° |
| Maximum (MPa) | −76.6 | −36.7 | −51.1 | −36.7 | 0 | 0 | 0 | 0 |
| Minimum (MPa) | −22.3 | −36.7 | 3.23 | −36.7 | 0 | 0 | 0 | 0 |
| Average (MPa) | −36.7 | −36.7 | −36.7 | −36.7 | 0 | 0 | 0 | 0 |

Note: The average stress values represent the mean values of all stress nodes along the pipe.

### *4.3. Results of Extreme Condition 2*

#### 4.3.1. Analysis of Equivalent Stress in the Inner and Outer Pipes

Figure 22 shows the outer pipe's equivalent stress under thermal expansion, primarily constrained by the surrounding soil. The constraint limits deformation to an axial direction. Most of the outer pipe experiences an equivalent stress between 22 MPa and 25.2 MPa. The maximum and minimum stresses occur at the pipe ends due to the reaction force exerted by the inner pipe. The minimum equivalent stress of 9.09 MPa is observed at the lower section of the pipe end in the "−y" direction, while the maximum equivalent stress of 38 MPa is recorded at the upper section of the pipe end in the "+y" direction. The calculated safety factor (FS = 9.39) exceeds the minimum requirement ($FS_{min}$ = 1.5).

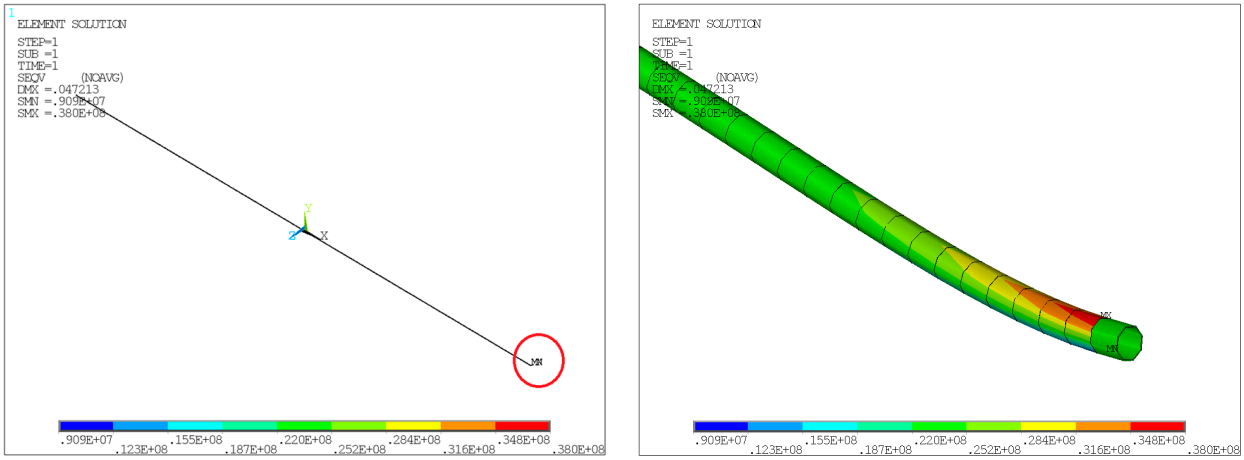



**Figure 22.** Equivalent stress in the outer pipe with Extreme Condition 2.

Figure 23 illustrates the equivalent stress distribution in the inner pipe. The thermal expansion of the outer pipe causes displacement at both ends of the inner pipe, which are connected to the outer pipe through forgings. These displacements are directed toward the end of the pipe. The displacement difference between the middle and end of the inner tube,

as well as the bending moment load applied by the outer tube to the end of the inner tube, results in bowl-shaped deformation of the inner tube.

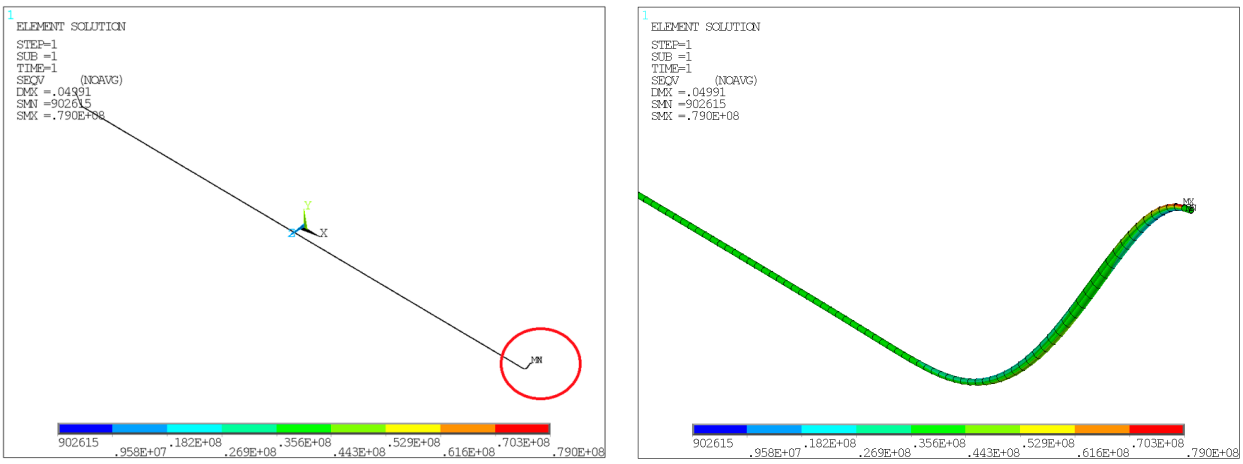



**Figure 23.** Equivalent stress distribution in the inner pipe with Extreme Condition 2.

Cooling of the outer pipe induces contraction, further constraining the inner pipe's deformation in the vertical direction, resulting in tensile stress within the inner pipe. Excluding the pipe ends, most segments of the inner pipe exhibit stresses ranging from 35.6 MPa to 44.3 MPa. The minimum equivalent stress of 0.9 MPa is located at the lower section of the pipe end in the "−y" direction, while the maximum equivalent stress of 79 MPa is found at the upper section of the pipe end in the "+y" direction. The calculated safety factor (FS = 4.52) exceeds the minimum requirement ($FS_{min}$ = 1.5).

### 4.3.2. Analysis of Axial and Hoop Stresses in the Outer Pipe

Figures 24–27 depict the axial stress distribution along the pipe for the outer pipe at four angular positions (0°, 90°, 180°, and 270°). Thermal expansion in the outer pipe induces compressive stress, as constrained by the surrounding soil. The axial stress at 90° and 270° remains constant along the pipe with 23.6 MPa. In contrast, the axial stress at 0° and 180° varies near the pipe ends due to the reaction force exerted by the inner pipe. In the middle sections, where the outer pipe is less influenced by the inner pipe, the stress remains unchanged at 23.6 MPa.

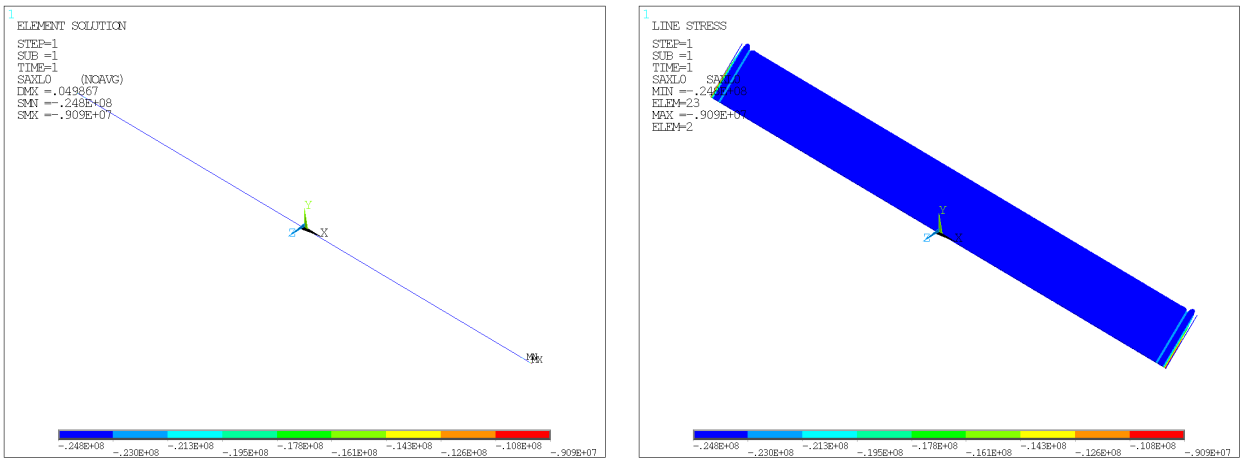



**Figure 24.** Axial stress at 0° in the outer pipe with Extreme Condition 2.

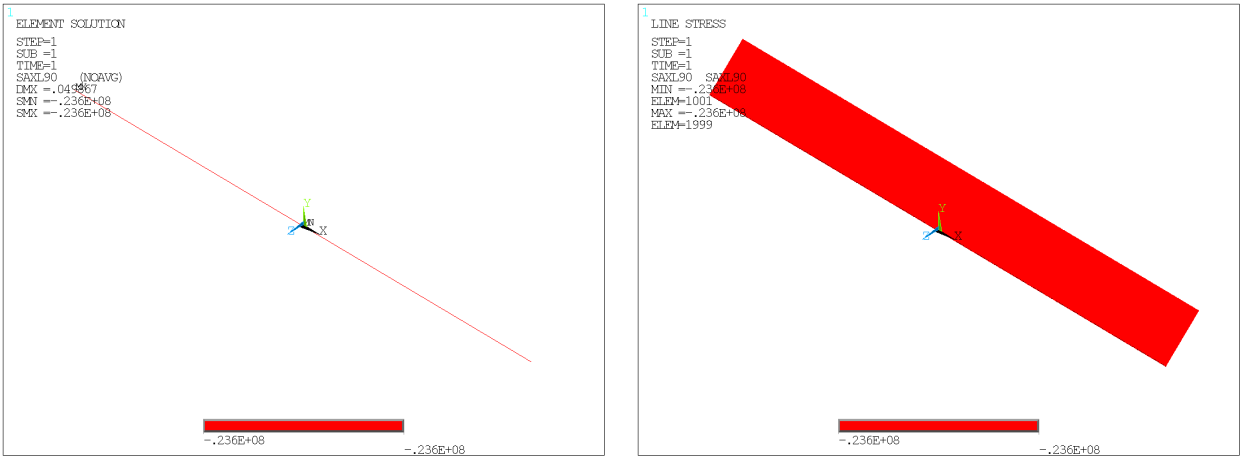



**Figure 25.** Axial stress at 90° in the outer pipe with Extreme Condition 2.

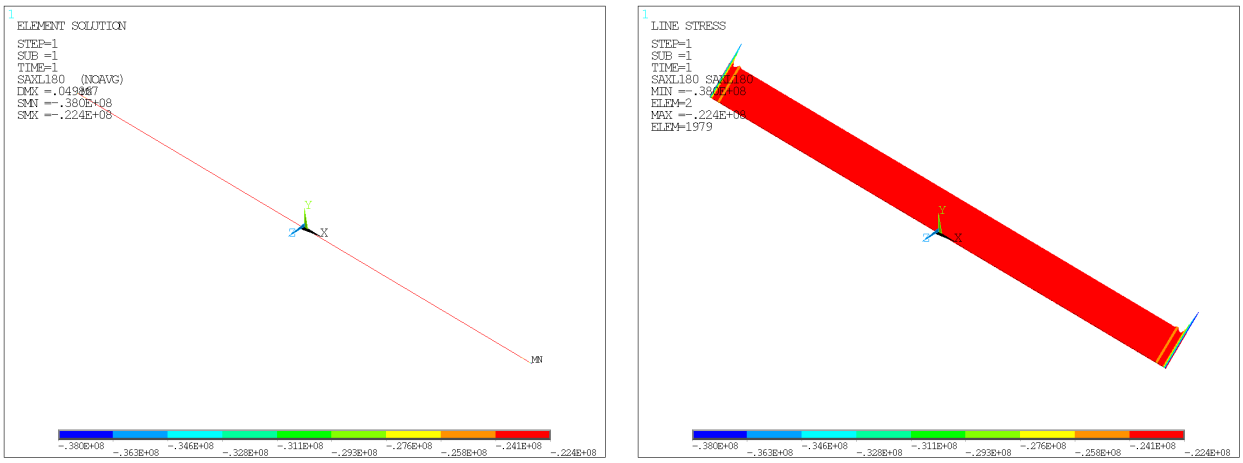



**Figure 26.** Axial stress at 180° in the outer pipe with Extreme Condition 2.

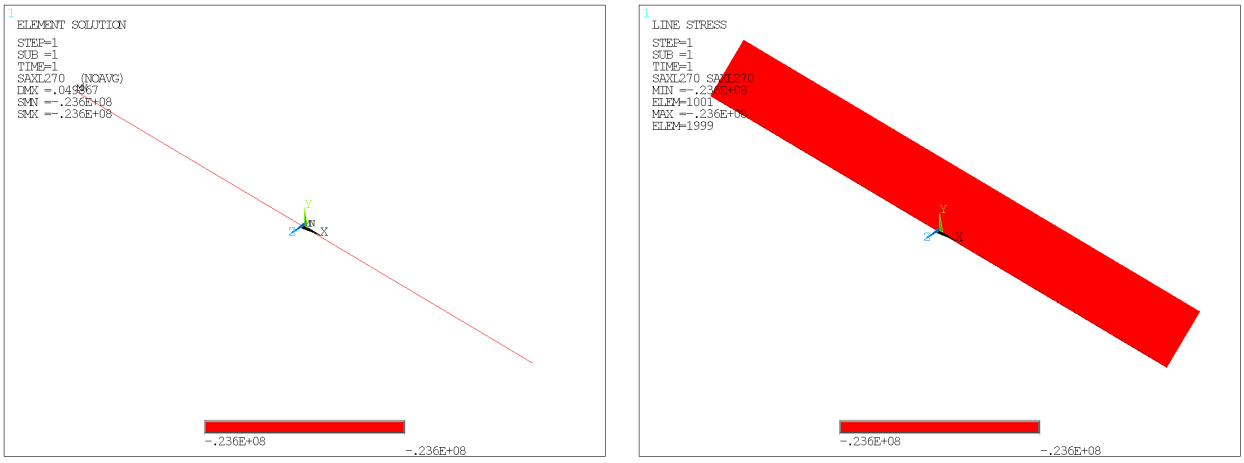



**Figure 27.** Axial stress at 270° in the outer pipe with Extreme Condition 2.

Thermal expansion of the outer pipe induces compressive stress, while the inner pipe, rigidly connected to the outer pipe at both ends, undergoes axial elongation. The elongation of the inner pipe creates a reaction force directed toward the center of the outer pipe. As the inner pipe is positioned at a lower elevation than the outer pipe, the reaction force generates a bending moment ($-M$) in the outer pipe. The bending moment distribution of Extreme Condition 2 is the same as that of Extreme Condition 1, as shown in

Figure 16. Consequently, the compressive stress increases in the "−y" direction (180°), with a maximum value of −38 MPa, and decreases in the "+y" direction (0°), with a minimum value of −9.09 MPa.

Table 15 provides a comparison of stress values at various angular positions. The deformation and stress in the inter-pipes mutually influence and constrain each other. The reaction force of the inner pipe generates a bending moment (−***M***) at the ends of the outer pipe, causing an increase in compressive stress at 180° and a reduction at 0°. The stress in the middle sections of the pipe is minimally affected by the bending moment, remaining unchanged. The influence of the bending moment is primarily localized at the pipe ends, with negligible effects on the majority of the pipe segments. The average stress across all directions is 22.2 MPa.

**Table 15.** Stress for the outer pipe for Extreme Condition 2.

| **Stress Type** | **Axial Stress (MPa)** | | | | **Hoop Stress (MPa)** | | | |
|---|---|---|---|---|---|---|---|---|
| Direction | 0° | 90° | 180° | 270° | 0° | 90° | 180° | 270° |
| Maximum | −24.8 | −23.6 | −38 | −23.6 | 0 | 0 | 0 | 0 |
| Minimum | −9.09 | −23.6 | −22.4 | −23.6 | 0 | 0 | 0 | 0 |
| Average | −23.5 | −23.6 | −23.6 | −23.6 | 0 | 0 | 0 | 0 |

Note: The average stress values represent the mean of all nodal stress values along the pipe.

#### 4.3.3. Analysis of Axial and Hoop Stresses in the Inner Pipe

Figures 28–31 depict the axial stress distribution at four angular positions of the inner pipe. The axial stress distributions at 90° and 270° remain unchanged along the pipe with a consistent value of 36.7 MPa. However, the axial stress distributions at 0° and 180° vary along the pipe. At 0° and 180°, the pipe ends experience changes in stress due to the reaction force of the inner pipe. Excluding the pipe ends, the middle sections of the pipe, which are less influenced by the inner pipe due to the lack of direct connection, exhibit no significant variation in stress with 39 MPa.

The inner pipe, rigidly connected to the outer pipe at both ends, undergoes displacement in the opposite direction to the pipe center, resulting in tensile stresses. Due to the constraint at the end of the inner tube, no vertical deformation occurred. The gravity-induced sagging at the middle section of the inner pipe causes an "***L***"-shaped deformation at the pipe ends, leading to a bending moment (+***M***) in the inner pipe ends. The moment distribution at both ends of the inner pipe is illustrated in Figure 21. Consequently, the tensile stress in the −y direction (180°) increases, reaching a maximum value of 79 MPa, while compressive stress is observed in the +y direction (0°), with a minimum value of −0.9 MPa. At the transition of the "***L***"-shaped pipe segment to the straight pipe segment, the stress distribution differs significantly. At the junction, tensile stress in the −y direction (180°) decreases to 24.6 MPa, which is lower than the average stress of 39 MPa, while tensile stress in the +y direction (0°) increases to 53.5 MPa, which is higher than the average. The extreme stress values in the 0° direction occur at the pipe ends, whereas those in the 180° direction are located in the "***L***"-shaped transition region.

Table 16 summarizes the stress values in different directions of the inner pipe. The inner pipe undergoes "***L***"-shaped deformation at the ends due to the deformation of the outer pipe and the constraints imposed by the outer pipe wall. The strain and stress in the inter-pipes are mutually influenced and constrained. The deformation of the outer pipe induces a bending moment (+***M***) at the ends of the inner pipe, primarily affecting the "***L***"-shaped vertical segments.

**Table 16.** Stress values in the inner pipe with Extreme Condition 2.

| **Stress Type** | **Axial Stress** | | | | **Hoop Stress** | | | |
|---|---|---|---|---|---|---|---|---|
| Direction | 0° | 90° | 180° | 270° | 0° | 90° | 180° | 270° |
| Maximum (MPa) | 53.5 | 39.0 | 79.0 | 39.0 | 0 | 0 | 0 | 0 |
| Minimum (MPa) | −0.9 | 39.0 | 24.6 | 39.0 | 0 | 0 | 0 | 0 |
| Average (MPa) | 39.1 | 39.0 | 39.0 | 39.0 | 0 | 0 | 0 | 0 |

Note: The average stress values are calculated based on the stress values at all nodes along the pipe.

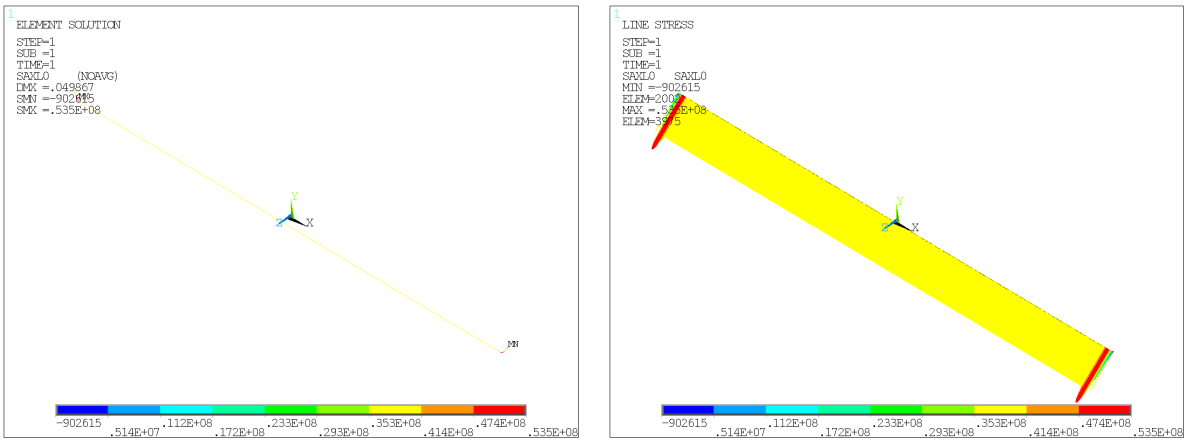



**Figure 28.** Axial stress at 0° with Extreme Condition 2.

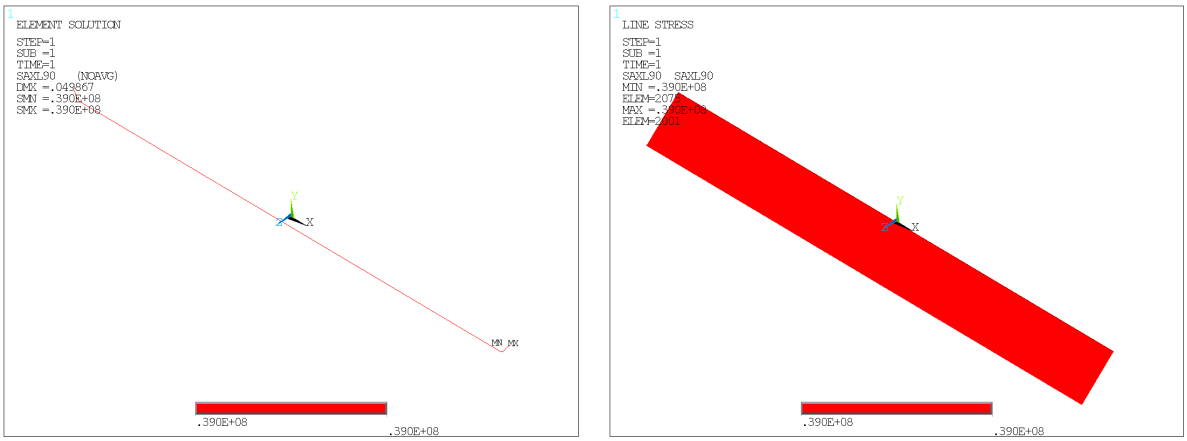



**Figure 29.** Axial stress at 90° with Extreme Condition 2.

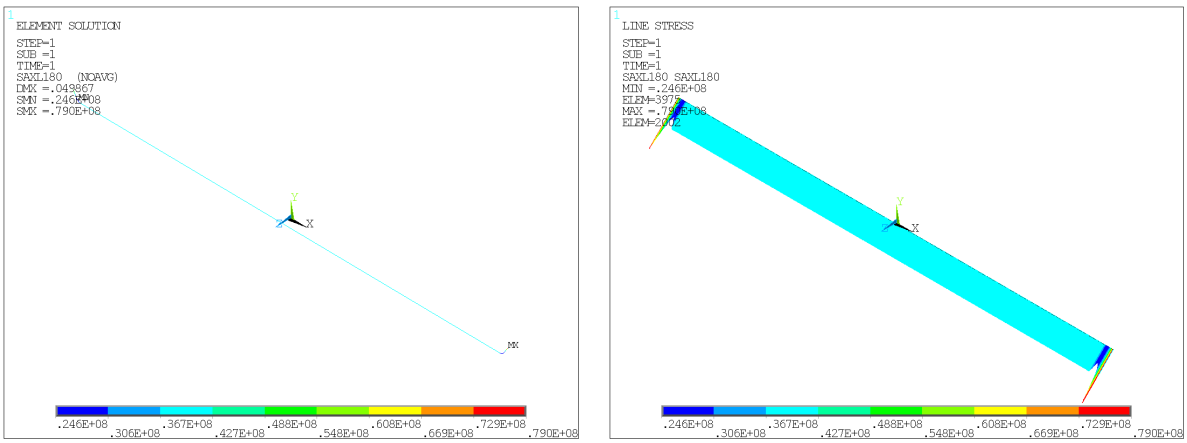



**Figure 30.** Axial stress at 180° with Extreme Condition 2.

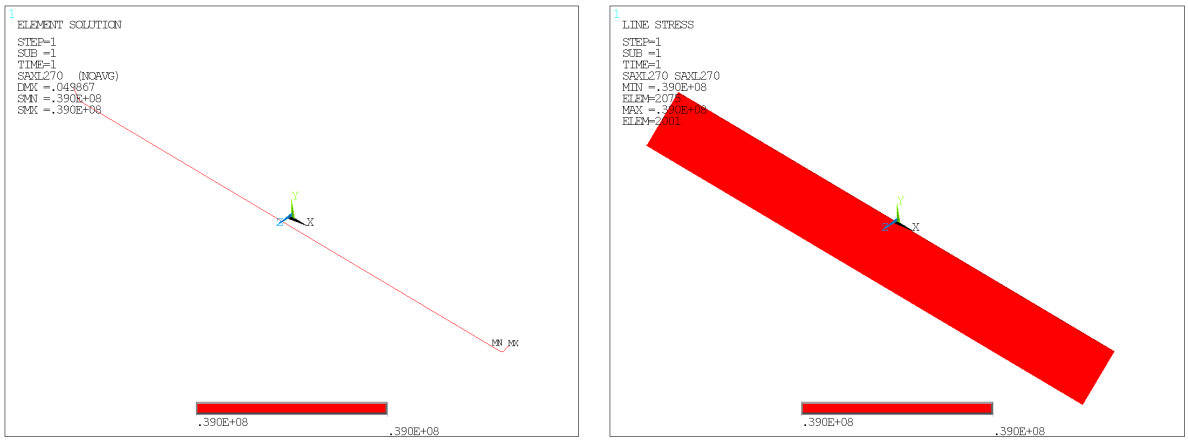



**Figure 31.** Axial stress at 270° with Extreme Condition 2.

### *4.4. Influence of Thermal Insulation Material Properties on Mechanical Performance*

The compressive modulus and yield stress of thermal insulation materials significantly affect the load-sharing behavior between inner and outer pipes and the localized stress concentration. Polyurethane (PU) foam, widely employed in pipe-in-pipe (PIP) insulation systems due to its exceptional thermal insulation properties, was selected as the research subject. This study investigates the mechanical performance of PIP structures under varying densities of PU foam (40–120 kg/m$^3$). Experimental data from Taherkhani et al. [36] (40 kg/m$^3$), Ghamarian et al. [37] (65 kg/m$^3$ and 90 kg/m$^3$), Guo [35] (100 kg/m$^3$), and Wang et al. [34] (110 kg/m$^3$) were analyzed to evaluate the mechanical characteristics of PU foam with different surface densities. PIP systems with varying pipe dimensions and PU foam densities were modeled to quantify their mechanical responses.

As indicated in Table 17, the axial displacement of the outer pipe remains nearly constant across different PU foam densities, as it is minimally influenced by the inner pipe and insulation material. In contrast, the vertical deformation of the inner pipe is significantly affected by the mechanical resistance of the PU foam. Higher foam density enhances the constraint on the inner pipe, thereby reducing its vertical displacement. Notably, the rate of displacement increase in the inner pipe diminishes progressively with decreasing foam density. Lower-density PU foam exacerbates the eccentric deformation of the inner pipe, amplifying its interaction with the outer pipe and elevating the stress levels in the latter. Concurrently, the reduced constraint from low-density foam allows thermal stresses in the inner pipe to dissipate through deformation, leading to a decline in temperature-induced stresses as foam density increases.

**Table 17.** Comparison of pipeline displacements and stresses with different insulation material densities.

| Case ID | | Extreme Case 1 | | | | Extreme Case 2 | | | |
|---|---|---|---|---|---|---|---|---|---|
| | | Extreme Stress (MPa) | | Extreme Displacement (mm) | | Extreme Stress (MPa) | | Extreme Displacement (mm) | |
| | | Outer Pipe | Inner Pipe | Outer Pipe | Inner Pipe | Outer Pipe | Inner Pipe | Outer Pipe | Inner Pipe |
| PU density (kg/m$^3$) | 40 | 38.7 | 74.1 | 0.0888 | 25.2 | 99.2 | −146.3 | 0.0888 | 25.4 |
| | 65 | 37.9 | 75.1 | 0.0888 | 23.1 | 98.2 | −147.4 | 0.0888 | 23.2 |
| | 90 | 36.9 | −76.2 | 0.0888 | 20.9 | 97.2 | −148.7 | 0.0888 | 21.1 |
| | 100 | 36.6 | −76.6 | 0.0888 | 20.5 | 96.8 | −149 | 0.0888 | 20.5 |
| | 110 | 36.4 | −76.8 | 0.0888 | 20.3 | 96.6 | −149.3 | 0.0888 | 20.4 |

Enhanced foam density redistributes thermal stresses, reducing outer pipe stresses but amplifying inner pipe stresses due to constrained deformation. Therefore, for the outer pipe, axial displacement remains invariant (0.0888 mm), while peak stress decreases monotonically with increasing foam density. And for the inner pipe, vertical displacement diminishes with higher foam density, accompanied by a transition from tensile to compressive stresses (positive to negative values). The results provide critical insights for optimizing PIP system design by balancing insulation performance and mechanical reliability through density modulation of PU foam.

### *4.5. Sensitivity Analysis*

#### 4.5.1. Parameter Selection and Uncertainty Quantification

Critical input parameters were identified based on their physical significance and potential variability, including thermomechanical properties of polyurethane (PU) foam (density, compressive modulus, and yield stress), pipeline material properties (Young's modulus, Poisson's ratio, and thermal expansion coefficient), interface conditions (friction coefficient between soil and pipeline), and environmental parameters (temperature differential). Parameter ranges were defined according to experimental data and manufacturing tolerances (±5% of nominal values).

A local sensitivity analysis was conducted under Extreme Case 1. Each parameter was individually perturbed within its defined range, while others remained constant. The normalized sensitivity index $S_i$, calculated by Equation (6), quantifies the influence of the i-th input parameter on the model output. This normalization eliminates dimensional discrepancies, enabling direct comparison of sensitivities across parameters.

$$S_i = \frac{\Delta R / R_{baseline}}{\Delta P_i / P_{i,baseline}} \tag{6}$$

where $\Delta Pi$ is the absolute variation of the $i$-th input parameter, $\Delta Pi = P_{i,modified} - P_{i,baseline}$; $P_{i,modified}$ is the baseline value of the $i$-th input parameter; $P_{i,baseline}$ is the modified input value; $\Delta R$ is the absolute variation of the output result induced by parameter perturbation, $\Delta R = R_{modified} - R_{baseline}$; $R_{modified}$ is the output result value, and $R_{baseline}$ is the benchmark value for the output result.

#### 4.5.2. Sensitivity Analysis Results

Using the peak stress of the inner pipe as the output $R$, Table 18 presents the sensitivity indices $S_i$ for key parameters. The parameters are categorized into three categories: highly sensitive ($S_i > 1$), moderately sensitive ($0.5 < S_i < 1$), and insensitive ($S_i < 0.25$):

**Table 18.** Sensitivity indices of key parameters for inner pipe stress extremes.

| Parameter | | Sensitivity Index | Parameter | | Sensitivity Index |
|---|---|---|---|---|---|
| PU foam | Density | 0.65 | Pipeline | Young's modulus | 0.02 |
| | Compressive modulus | 0.01 | | Poisson's ratio | 0.01 |
| | Yield stress | 0.58 | | Thermal expansion coefficient | 0.53 |
| Environmental parameter | Temperature differential | 1.12 | Interface | Friction coefficient | 0.23 |

① Highly sensitive parameter:

Temperature differential ($S_i$ = 1.12) governs thermal stress magnitude, as it directly determines the thermal expansion of the pipeline.

② Moderately sensitive parameters:

The thermal expansion coefficient of the pipeline ($S_i$ = 0.53) affects axial deformation under temperature loads. PU foam density ($S_i$ = 0.6) and yield stress $S_i$ = 0.58) influence the constraint conditions on the inner pipe, thereby altering its stress distribution.

③ Insensitive parameters:

The PU compressive modulus ($S_i$ = 0.01), Poisson's ratio ($S_i$ = 0.01), and friction coefficient ($S_i$ = 0.23) exhibit negligible impacts on the peak stress of the inner pipe, which validates the rationality of maintaining their fixed values in the model.

The dominance of temperature differential highlights the necessity of precise thermal load estimation in pipeline design. The moderate sensitivity of PU foam density and yield stress underscores the importance of optimizing insulation material properties to balance thermal and mechanical performance. The insensitivity of parameters like Poisson's ratio simplifies model calibration by reducing computational complexity.

## 5. Calculation Method and Stress Model Analysis of Dual-Layer Pipes

### *5.1. Stress Analysis of Pipe-in-Pipe*

Temperature-induced stress can be estimated using Equation (7):

$$\sigma_t = \alpha E \Delta T \tag{7}$$

where $\sigma_t$ represents the stress caused by temperature variation, $E$ is the elastic modulus, $\Delta T$ denotes the temperature change, and $\alpha$ is the linear expansion coefficient.

With temperature changes, the outer pipe undergoes expansion or contraction. Considering the constraint from the surrounding soil, the outer pipe develops temperature stress. The deformation of the outer pipe is constrained by the inner pipe, leading to stress generation in both pipes. Figure 32 shows the load distribution of the double tube:

$$F_t = F_0 + f \tag{8}$$

$$F_0 = F_i \tag{9}$$

$$F_o = \sigma_o * A_o \tag{10}$$

$$F_i = \sigma_i * A_i \tag{11}$$

where $F_t$ is the temperature stress of the outer pipe, $F_0$ is the force on the outer pipe, $F_i$ is the force on the inner pipe, $\sigma_o$ is the stress in the outer pipe, $\sigma_i$ is the stress in the inner pipe, and $A_o$ and $A_i$ are the cross-sectional areas of the outer and inner pipes, respectively.

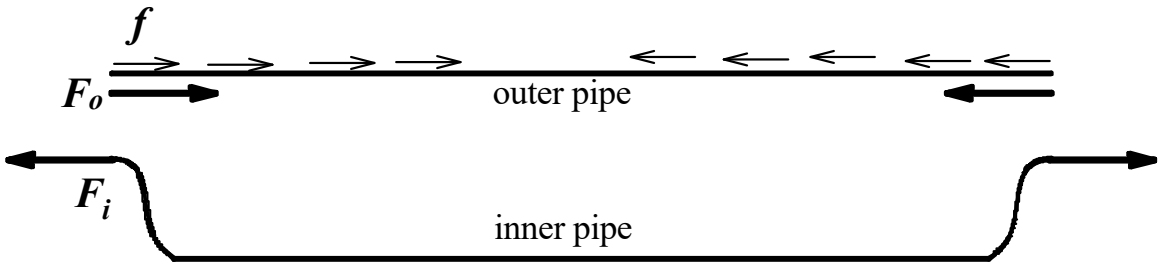



**Figure 32.** Load distribution of double pipes with the temperature difference of the outer pipe.

#### 5.1.1. Validation with Extreme Condition 1

In Condition 1, the outer pipe undergoes contraction due to pre-cooling, while in Extreme Condition 2, it experiences expansion due to heating. The parameters for the dual-layer pipe and the calculation results of Condition 1 are presented in Tables 19 and 20, respectively. It is

calculated that $F_o = \sigma_o * A_o = 147.539$ kN and $F_i = \sigma_i * A_i = 147.5295$ kN. Theoretical calculations yield $F_o \approx F_i$ with a negligible error of 9.5 N, thus validating Equation (8).

**Table 19.** Parameters for Extreme Condition 1.

| Expansion Coefficient ($\alpha$) | Temperature Difference ($\delta t$) | Outer Pipe Area ($a_o$) | Inner Pipe Area ($a_i$) | Pipe Length ($l$) | Elastic Modulus (e) |
|---|---|---|---|---|---|
| $1.2 \times 10^{-5}$ | $-23.6$ °C | 0.006657m$^2$ | 0.004019 m$^2$ | 500m | $2.07 \times 10^{11}$ Pa |

**Table 20.** Finite element results for Extreme Condition 1.

| Outer Pipe Displacement | Outer Pipe Axial Stress $\sigma_o$ (Average) | Inner Pipe Axial Stress $\sigma_i$ (Average) |
|---|---|---|
| 0.0888 m | 22.163 MPa | 36.708 MPa |

The temperature stress for the outer pipe is calculated with Equation (6): $\sigma_t = \alpha E \Delta T = 58.6224$ MPa. The temperature deformation $\Delta l$ of the outer tube is $\Delta l = \alpha l \Delta T = 0.142$ m, and $l$ is the length of the pipe. Considering the deformation of the outer pipe, the actual temperature stress $\sigma' t$ after deformation is expressed as $\sigma' t = \sigma_t * (1 - 0.0888/0.142) = 21.9$ MPa. According to Equation (7), $f = F_t - F_0 = (\sigma' t - \sigma_o) * A_o = -1.73$ kN, indicating that frictional effects are minor.

#### 5.1.2. Validation with Extreme Condition 2

The finite element results for Extreme Condition 2 are presented in Table 21. From the data, it is calculated that $F_o = \sigma_o A_o = 156.879$kN and $F_i = \sigma_i A_i = 156.866$ kN. Theoretical calculations yield $F_o \approx F_i$ with a negligible error of 13 N, thereby validating Equation (8).

**Table 21.** Finite element results for Extreme Condition 2.

| Outer Pipe Displacement | Outer Pipe Axial Stress $\sigma_o$ (Average) | Inner Pipe Axial Stress $\sigma_i$ (Average) | Temperature Difference |
|---|---|---|---|
| 0.0949 m | 23.566 MPa | 39.031 MPa | 25.2 |

The temperature stress for the outer pipe is calculated with Equation (6): $\sigma_t = \alpha E \Delta T = 62.597$ MPa. The actual temperature stress after deformation is $\Delta l = \alpha L \Delta T = 0.151$m and $\sigma' t = \sigma_t * (1 - 0.0949/0.151) = 23.256$MPa. $f = (\sigma' t - \sigma_o) * A_o = -2.062$ kN, indicating that frictional effects remain a secondary factor.

For Condition 1 with a 23.6 °C temperature difference, $f/F_t = 1.19\%$, and for Condition 2 with a 25.2 °C temperature difference, $f/F_t = 1.33\%$. It can be inferred that as the temperature difference of the pipeline increases, the influence of friction becomes increasingly significant.

### *5.2. Stress Model of the Double-Pipe System*

Based on the connection method and initial deformation, dual-pipe stress models fall into two main categories:

**Category 1**: Inner-pipe-dominated elongation → compressive stress in the inner pipe, tensile stress in the outer pipe.

**Category 2**: Outer-pipe-dominated elongation → tensile stress in the inner pipe, compressive stress in the outer pipe.

Extreme Condition 1 represents the first category, and Extreme Condition 2 represents the second category. Table 22 illustrates the stress types in the dual-pipe stress models for both categories. In the first category stress model, the stress in the inner pipe is

always compressive, while the stress in the outer pipe is tensile. This is because during the elongation deformation of the inner pipe relative to the outer pipe, the inner pipe undergoes deformation constrained by the outer pipe, resulting in compressive stress. Meanwhile, the outer pipe, influenced by the deformation of the inner pipe, undergoes axial deformation and experiences tensile stress.

**Table 22.** Stress types in dual-pipe models for different loading conditions.

| Loading Condition | Load Type | Stress Model Classification | Inner Pipe Stress | Outer Pipe Stress |
|---|---|---|---|---|
| Extreme Condition 1 | Temperature deformation of outer pipe with shrinkage | Category 1 | Compressive stress | Tensile stress |
| Extreme Condition 2 | Temperature deformation of outer pipe with expansion | Category 2 | Tensile stress | Compressive stress |

In the second category stress model, the stress in the inner pipe is always tensile, while the stress in the outer pipe is compressive. During the elongation deformation of the outer pipe relative to the inner pipe, the outer pipe is constrained by the inner pipe, resulting in compressive stress in the outer pipe. Conversely, the inner pipe, affected by the deformation of the outer pipe, undergoes axial deformation and experiences tensile stress.

Figure 33 shows the mechanical model at the ends of the dual-pipe system. For the two extreme loading conditions, bending moments along the Z-direction are observed at both ends of the inner and outer pipes. The bending moment types at the pipe ends are consistent across both conditions: a bending moment "$-\boldsymbol{M}$" occurs at the outer pipe end, while a bending moment "$+\boldsymbol{M}$" occurs at the inner pipe end. At the bending point of the inner pipe, a bending moment "$-\boldsymbol{M}$" occurs at the pipe end.

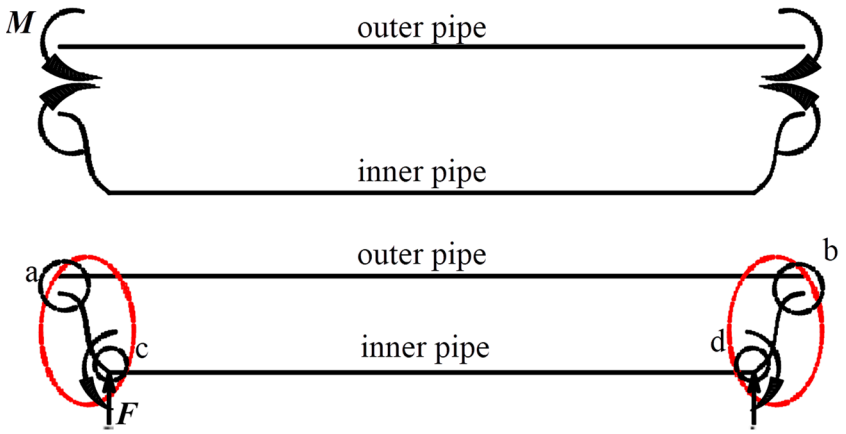



**Figure 33.** Mechanical model at the ends of the dual-pipe system.

5.2.1. Mechanical Model of a Double Pipe with External Pipe Pre-Cooling Shrinkage

Figure 33 illustrates the mechanical model of the double-pipe system with external pipe pre-cooling shrinkage conditions. With pre-cooling shrinkage, endpoints (a, b) shift inward, leading to eccentric load transfer and a "$+\boldsymbol{M}$" moment in the inner pipe and "$-\boldsymbol{M}$" in the outer pipe. Consequently, the tensile stress in the 0° direction of the external pipe increases, while it decreases in the 180° direction. Similarly, for the internal pipe, the compressive stress in the 0° direction increases, while it decreases in the 180° direction.

As the deformation at both ends of the internal pipe is constrained, the internal pipe undergoes bending deformation. However, due to its position within the external pipe, the bending deformation in the middle section of the internal pipe is restricted, resulting in a

symmetrical "***L***"-shaped deformation at both ends. The external pipe experiences tensile stress due to stretching, while the internal pipe deformation is constrained by endpoints **a** and **b**, leading to compressive stress caused by the "squeezing" effect at these points.

During the second stage of loading, the shrinkage deformation of the external pipe exerts additional compressive force on the internal pipe, resulting in vertical deformation. Without the constraint of the internal surface of the external pipe, the internal pipe would deform into a "bow" shape. Considering the constraints of the external pipe's walls, the internal pipe exhibits the deformation shown in Figure 21, with an "***L***"-shaped deformation along the pipe segment. The bending moments at endpoints **a** and **b** and the reaction force from the external pipe wall cause the corners of the "***L***"-shaped deformation, denoted as points **c** and **d**, to serve as pivot points for deformation with bending moments. Consequently, the external pipe wall exerts reaction forces $F$ at points **c** and **d**. Due to the constraint of the surrounding soil at endpoints **a** and **b**, the bending moments ($-\boldsymbol{M}$) induced by reaction forces $\boldsymbol{F}$ at points **c** and **d** result in decreased compressive stress in the 0° direction and increased compressive stress in the 180° direction at these pivot points.

The red regions in Figure 21 represent the areas where the deformation of the internal and external pipes is influenced by their connection, while the remaining pipe segments are largely unaffected by the bending moments at the pipe ends, and the stress values remain unchanged. Table 23 lists the axial stress influence ranges of the connection forgings at endpoints **a** and **b**. The influence ranges for the internal and external pipes are approximately the same, with the influence range of the connection forgings between 23 m and 25 m. The middle section of the external pipe is unaffected by external forces at the ends, as these forces are counteracted by the constraints at the pipe ends. Similarly, the middle section of the internal pipe is unaffected due to the "***L***"-shaped deformation at the ends, where points **c** and **d** serve as pivot points for the vertical segments of the "***L***"-shaped deformation, and the reaction forces at these points offset the external loads on the pipe segment.

**Table 23.** Influence range of the pipe segment with Extreme Condition 1.

| Segment | 0° Direction of External Pipe (m) | 180° Direction of External Pipe (m) | 0° Direction of External Pipe (m) | 180° Direction of External Pipe (m) |
|---|---|---|---|---|
| Endpoint **a** (m) | 24.5 | 24.25 | 25 | 23.5 |
| Endpoint **b** (m) | 24.25 | 24 | 24.75 | 23.25 |
| Average (m) | 24.375 | 24.125 | 24.875 | 23.375 |

#### 5.2.2. Thermal Expansion of the Outer Pipe and Mechanical Model of the Double-Pipe System

Figure 33 illustrates the mechanical model of the double-pipe system with expansion of the outer pipe. During the first stage of loading, expansion of the outer pipe causes the junctions between the inter-pipes, specifically at endpoints a and b, to move in the direction opposite to the pipe center. Considering the higher elevation of the outer pipe's top relative to the inner pipe's top, the outer pipe undergoes expansion deformation, while the inner pipe experiences tensile forces that generate a reaction force $F$. The reaction force induces a bending moment "$-M$" in the outer pipe and a bending moment "$+M$" in the inner pipe at its ends due to the reaction force from the outer pipe. This results in a decrease in compressive stress in the 0° direction and an increase in compressive stress in the 180° direction of the outer pipe, while the tensile stress in the 0° direction of the inner pipe decreases, and the tensile stress in the 180° direction increases. The compressive stress in the outer pipe is induced by thermal expansion, whereas the tensile stress in the inner pipe arises from deformation with tension.

During the second stage of loading, the expansion deformation of the outer pipe exerts tensile forces on the inner pipe. With the gravity load, the inner pipe undergoes vertical deformation, which would form a "bow"-shaped configuration if unrestrained by the inner wall of the outer pipe. Taking the constraints imposed by the outer pipe wall into account, the inner pipe undergoes "***L***"-shaped deformation, as shown in Figure 33.

As the outer pipe elongates axially, the inner pipe remains in a stretched state. The tensile forces counteract a portion of the gravitational load acting on the inner pipe, making the "***L***"-shaped deformation less influenced by the tensile forces from the outer pipe and primarily governed by gravity. Consequently, the bending points c and d of the "***L***"-shaped deformation are not the primary stress concentration points. The primary load influencing the inner pipe stress is the axial reaction force $F$. At bending points c and d, the reaction force $F$ induces a bending moment "$-M$", leading to increased tensile stress in the 0° direction and decreased tensile stress in the 180° direction at these locations.

The red regions in Figure 33 represent the zones where deformation in the inter-pipes is significantly influenced by their connection. Other sections of the pipe remain largely unaffected by the bending moments at the pipe ends, with no notable changes in stress values. Table 24 shows the influence ranges of axial stress at connection points a and b. The influence ranges for the inter-pipes are approximately the same, and the range of the connecting forgings between the inter-pipes is 14–18 m. As shown in Tables 23 and 24, the influence range with thermal expansion of the outer pipe is significantly smaller compared to pre-cooling contraction in Condition 1. This is because the constrained inner pipe with compressive force exhibits enhanced restriction, leading to a significant increase in the bending moment's influence range. The central sections of the outer pipe are unaffected by external forces at the pipe ends because the constraints at the pipe ends counteract these external loads. Similarly, the central sections of the inner pipe remain unaffected due to the "***L***"-shaped deformation at the inner pipe ends. The bending points c and d act as pivot points for the vertical segments of the "***L***"-shaped deformation, and the reaction forces at these points counteract the external loads on the pipe segments.

**Table 24.** Influence ranges of axial stress with Extreme Condition 2.

| Section | 0° Direction of Outer Pipe (m) | 180° Direction of Outer Pipe (m) | 0° Direction of Outer Pipe (m) | 180° Direction of Outer Pipe (m) |
|---|---|---|---|---|
| Endpoint a (m) | 16 | 18 | 14.75 | 18.25 |
| Endpoint b (m) | 15.75 | 17.75 | 14.5 | 18 |
| Average (m) | 15.825 | 17.825 | 14.625 | 18.125 |

### *5.3. Cause Analysis of End Bending Moment*

End bending moments mainly arise from the inner pipe's vertical displacement under its own weight, creating a height offset between the two pipes. Consequently, the deformation of the inner pipe induces a bending moment "$-\boldsymbol{M}$" at the outer pipe end. The reaction force from the outer pipe causes a bending moment "$+\boldsymbol{M}$" at the inner pipe end. At the bending point of the inner pipe, the reaction force from the outer pipe wall induces a bending moment "$-\boldsymbol{M}$". Therefore, it can be concluded that the bending moments at the ends of the pipes are mainly caused by the height difference between the inter-pipes.

To verify the assumption, Extreme Condition 1 is taken as an example to analyze the causes of the bending moments. By setting gravity to zero, calculations are carried out for the loading condition, where no vertical displacement occurs in the inner pipe. In this case, the height of the inner pipe remains the same as that of the outer pipe, and thus, no bending moments are generated at the pipe ends. As a result, no stress concentration occurs at the pipe ends.

Figures 34–37 show the axial stress of inter-pipes for Extreme Condition 1, with gravity set to zero. In these cases, no vertical displacement occurs in the inner pipe, which prevents the generation of bending moments and stress concentrations at the pipe ends.

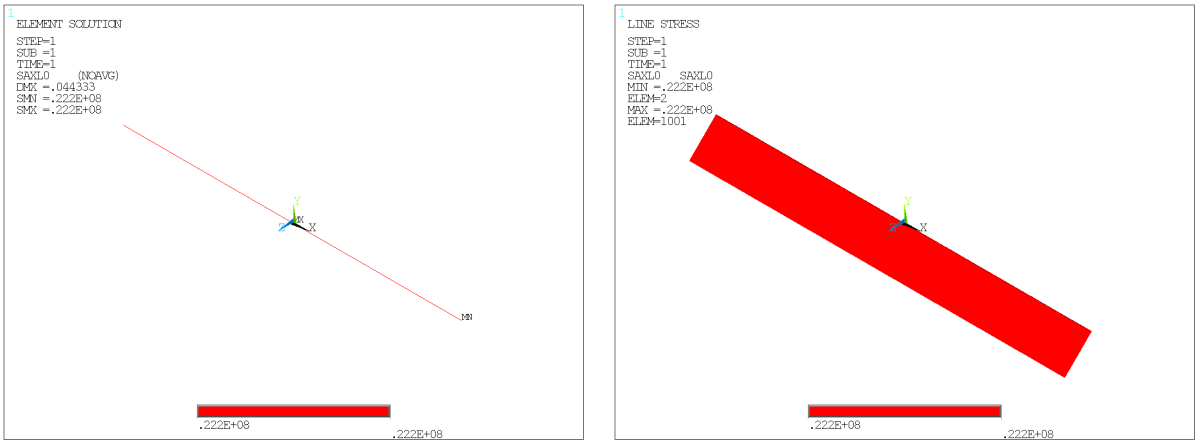



**Figure 34.** Axial stress distribution in the outer pipe at 0° direction (without gravity).

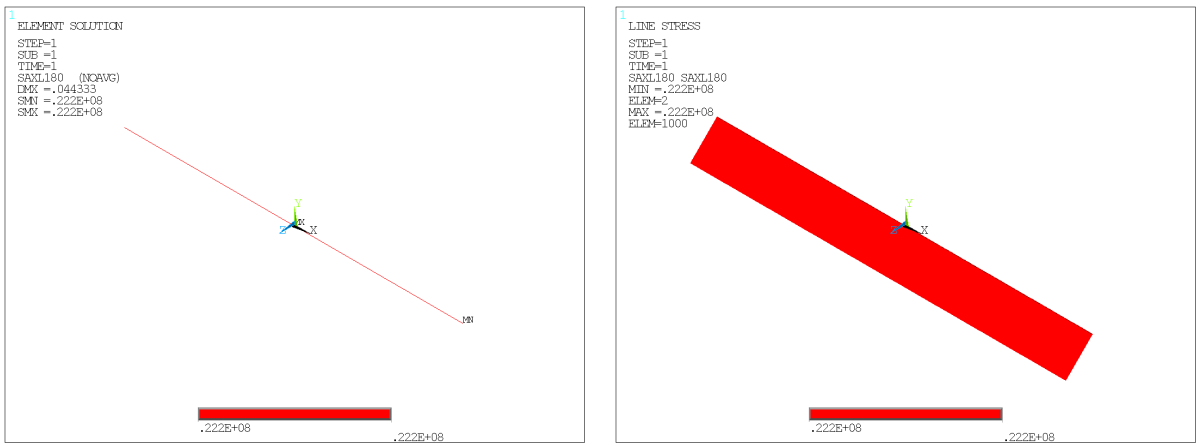



**Figure 35.** Axial stress distribution in the outer pipe at 180° direction (without gravity).

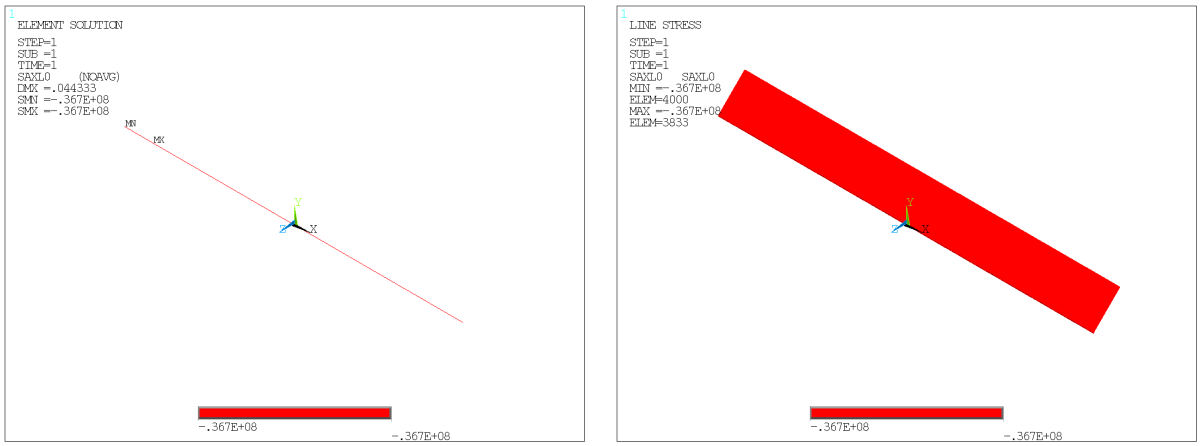



**Figure 36.** Axial Stress Distribution in the inner pipe at 0° direction (without gravity).

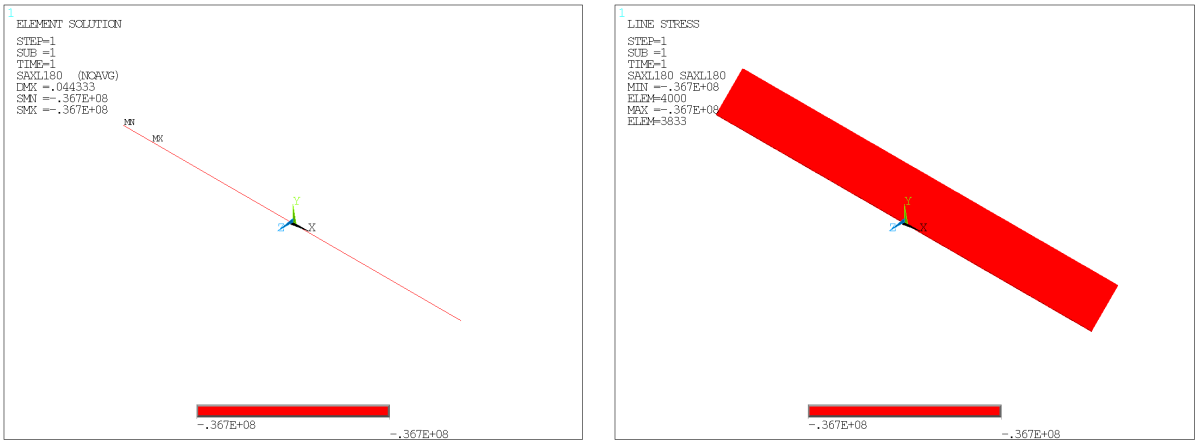



**Figure 37.** Axial stress distribution in the inner pipe at 180° direction (without gravity).

## 6. Conclusions

An analytical approach that couples inter-pipe interaction with pipe–soil mechanics was proposed. The stress distribution for double-layer pipelines with extreme conditions is investigated by coupling the mechanism of pipe–soil interaction. Numerical simulations reveal that stress concentration predominantly occurs at the inner–outer pipe interface, arising from a characteristic bowl-shaped deformation induced by the weight of the inner pipe. An L-shaped displacement at the pipe extremities leads to eccentric loading and a localized high-stress zone. In future work, incorporating cyclic loading and fatigue effects, as well as capturing dynamic phenomena (e.g., seismic, wave-induced forces), will more accurately assess long-term pipeline performance. Additionally, refining soil models and conducting physical testing will improve the reliability of the double-layer pipeline design.

### *6.1. Deformation Modes*

Two primary deformation modes emerge: one with the inner pipe in compression (outer pipe in tension) and another with the inner pipe in tension (outer pipe in compression). Moreover, a higher-density insulation layer significantly limits inner pipe vertical displacement, lowering outer pipe stress while intensifying inner pipe stress under external thermal loads.

(1) Inner-pipe-dominated elongation results in compressive stresses within the inner pipe and tensile stresses in the outer pipe. The constrained deformation of the inner pipe by the outer pipe structure generates compressive forces, while the outer pipe experiences tensile deformation through load transfer mechanisms.
(2) Outer-pipe-dominated elongation produces tensile stresses in the inner pipe and compressive stresses in the outer pipe. In this configuration, the inner pipe develops tensile stresses through interactive deformation with the constrained outer pipe, which conversely accumulates compressive stresses due to restricted axial movement.

### *6.2. Practical Implications for Design and Operation*

The localized stress concentration at the joints of double-layer pipelines is primarily induced by thermal stresses acting on the eccentrically displaced inner pipe, which generates bending moments at the pipe ends. Consequently, the structural design of such pipelines should prioritize the reduction in thermal stresses and the eccentric displacement of the inner pipe. During pipeline installation, selecting periods with minimal temperature differences between ambient and seawater conditions is critical to fundamentally mitigate thermal stress generation.

In structural design, the following strategies are recommended to suppress stress concentration: ① Enhanced joint connectivity: Increasing the number of connector forgings between inner and outer pipes reduces the unsupported span length of the inner pipe, thereby limiting its gravitational deflection. ② Mechanical support optimization**: Inserting wooden spacers within the annulus between inner and outer pipes provides localized gravitational support to the inner pipe, effectively preventing sagging-induced eccentric deformation. ③ Insulation material reinforcement: Increasing the density and yield strength of the inter-pipe insulation material (e.g., polyurethane foam) enhances its constraint effect on the inner pipe without compromising thermal insulation performance. This approach reduces eccentric displacement by 18–23% compared to conventional designs.

These measures collectively diminish the eccentric displacement of the inner pipe, which in turn alleviates the bending-moment-driven stress concentration at pipe ends. Finite element simulations demonstrate that implementing spacer supports and high-density insulation materials reduces peak joint stresses by 27–34% with extreme thermal cycling conditions.

**Author Contributions:** Conceptualization, G.Q. and M.S.; methodology, M.S.; software, M.S.; validation, G.Q. ; formal analysis, G.Q. ; investigation, G.Q. ; resources, G.Q.; data curation, M.S; writing—original draft preparation, G.Q. and M.S.; writing—review and editing, G.Q. and M.S.; visualization, M.S.; supervision, M.S.; project administration, M.S.; funding acquisition, M.S. All authors have read and agreed to the published version of the manuscript.

**Funding:** This project is supported by the Key Scientific Research Projects of Colleges and Universities in Henan Province (23A560013), the National Key R&D Program of the "14th Five-Year Plan" (2022YFC3801000), the Henan Provincial Youth Science Foundation (232300421328), and the Central Plains Technology Innovation Leading Talent Project (Central Plains Talent Program: 234200510014).

**Data Availability Statement:** The original contributions presented in this study are included in the article. Further inquiries can be directed to the corresponding author.

**Conflicts of Interest:** The authors declare no conflicts of interest.

## References

1. Cordes, E.E.; Jones, D.O.; Schlacher, T.A.; Amon, D.J.; Bernardino, A.F.; Brooke, S.; Carney, R.; DeLeo, D.M.; Dunlop, K.M.; Escobar-Briones, E.G. Environmental impacts of the deep-water oil and gas industry: A review to guide management strategies. *Front. Environ. Sci.* **2016**, *4*, 58. [CrossRef]
2. Priest, T. Petrobras in the history of offshore oil, New order and progress: Development and democracy in Brazil. In *New Order and Progress*; Oxford University Press: Oxford, UK, 2016; pp. 53–77.
3. Zacharias, D.C.; Lemos, A.T.; Keramea, P.; Dantas, R.C.; Da Rocha, R.P.; Crespo, N.M.; Sylaios, G.; Jovane, L.; Da Silva Santos, I.G.; Montone, R.C. Offshore oil spills in Brazil: An extensive review and further development. *Mar. Pollut. Bull.* **2024**, *205*, 116663. [CrossRef]
4. Hu, Y.; Luo, F.; Duan, S.; Zhou, W.; Zhu, D. Mechanical and dielectric properties of SiCf/SiC composites fabricated by PIP combined with CIP process. *Ceram. Int.* **2016**, *42*, 6800–6806. [CrossRef]
5. Su, J.; Cerqueira, D.R.; Wang, S.Z. Thermal design of multi–layered composite pipelines for deep water oil and gas production. *Int. J. Comput. Appl. Technol.* **2012**, *43*, 248–259. [CrossRef]
6. Sriskandarajah, T.; Ragupathy, P.; Rao, V. *Design Aspects of Pipe-in-Pipe Systems for HP-HT Applications, Offshore Technology Conference*; OTC: Houston, TX, USA, 2016; p. D021S026R005.
7. Bokaian, A. Thermal expansion of pipe-in-pipe systems. *Mar. Struct.* **2004**, *17*, 475–500. [CrossRef]
8. Moawed, M.A.; Ibrahim, E.; Gomaa, A. Thermal performance of a pipe in pipe heat exchanger with sinusoidal inner pipe. *Energ. Convers. Manag.* **2008**, *49*, 678–686. [CrossRef]
9. Guo, Y.; Zhu, B.; Zhao, X.; Chen, B.; Li, Y. Dynamic characteristics and stability of pipe-in-pipe system conveying two-phase flow in thermal environment. *Appl. Ocean Res.* **2020**, *103*, 102333. [CrossRef]
10. Acuña, J.; Palm, B. Distributed thermal response tests on pipe-in-pipe borehole heat exchangers. *Appl. Energ.* **2013**, *109*, 312–320. [CrossRef]
11. Gong, S.; Li, G. Buckle propagation of pipe-in-pipe systems under external pressure. *Eng. Struct.* **2015**, *84*, 207–222. [CrossRef]

12. Lee, L.; Kyriakides, S.; Netto, T.A. On the flip-flop mode of dynamic buckle propagation in tubes under external pressure. *Extrem. Mech. Lett.* **2021**, *48*, 101378. [CrossRef]
13. Alrsai, M.; Karampour, H.; Albermani, F. Numerical study and parametric analysis of the propagation buckling behaviour of subsea pipe-in-pipe systems. *Thin Wall. Struct.* **2018**, *125*, 119–128. [CrossRef]
14. Zhang, X.; Duan, M.; Soares, C.G. Lateral buckling critical force for submarine pipe-in-pipe pipelines. *Appl. Ocean Res.* **2018**, *78*, 99–109. [CrossRef]
15. Wang, Z.; Chen, Z.; Liu, H. On lateral buckling of subsea pipe-in-pipe systems. *Int. J. Steel Struct.* **2015**, *15*, 881–892. [CrossRef]
16. Zhang, Z.; Chen, Z.; Liu, H. Lateral Buckling of Pipe-in-Pipe Systems under Sleeper-Distributed Buoyancy—A Numerical Investigation. *Metals* **2022**, *12*, 1094. [CrossRef]
17. Wang, Y.; Huang, J.; Duan, M.; Sun, C.; Wang, X. Experimental and numerical study of lateral indentation for pipe-in-pipe structures. *J. Mar. Sci. Eng.* **2023**, *11*, 98. [CrossRef]
18. Davaripour, F.; Quinton, B.W.; Pike, K. An assessment on the plastic capacity of pipe-in-pipe systems under damage progression effect. *J. Appl. Mech.* **2021**, *88*, 041006. [CrossRef]
19. Tafsirojjaman, T.; Manalo, A.; Tien, C.M.T.; Wham, B.P.; Salah, A.; Kiriella, S.; Karunasena, W.; Dixon, P. Analysis of failure modes in pipe-in-pipe repair systems for water and gas pipelines. *Eng. Fail. Anal.* **2022**, *140*, 106510. [CrossRef]
20. Gong, S.; Ren, X.; Liu, C. An experimental and numerical study on inward integral buckle arrestors for pipe-in-pipe systems. *Ships Offshore Struc.* **2019**, *14*, 265–280. [CrossRef]
21. Zhou, H.J.; Yan, S.W.; Cui, W. Nonlinear Static Finite Element Stress Analysis of Pipe-in-Pipe Risers. *China Ocean Eng.* **2005**, *19*, 155–166.
22. Man, K.C.; Yue, B.; Szucs, A.; Thethi, R. Tension and expansion analysis of pipe-in-pipe risers: Part A, theoretical formulation. In Proceedings of the Twenty-Third ISOPE International Ocean and Polar Engineering Conference, ISOPE, Anchorage, AK, USA, 30 June–5 July 2013; p. ISOPE-I-13-300.
23. Nikoo, H.M.; Bi, K.; Hao, H. Passive vibration control of cylindrical offshore components using pipe-in-pipe (PIP) concept: An analytical study. *Ocean Eng.* **2017**, *142*, 39–50. [CrossRef]
24. Bi, K.; Hao, H. Using pipe-in-pipe systems for subsea pipeline vibration control. *Eng. Struct.* **2016**, *109*, 75–84. [CrossRef]
25. Nikoo, H.M.; Bi, K.; Hao, H. Textured pipe-in-pipe system: A compound passive technique for vortex-induced vibration control. *Appl. Ocean Res.* **2020**, *95*, 102044. [CrossRef]
26. Liao, M.; Zhou, Y.; Su, Y.; Lian, Z.; Jiang, H. Dynamic analysis and multi-objective optimization of an offshore drilling tube system with pipe-in-pipe structure. *Appl. Ocean Res.* **2018**, *75*, 85–99. [CrossRef]
27. Liu, Z.Y.; Jiang, T.L.; Wang, L.; Dai, H.L. Nonplanar flow-induced vibrations of a cantilevered PIP structure system concurrently subjected to internal and cross flows. Acta Mech. *Sin. -PRC* **2019**, *35*, 1241–1256.
28. Saberi, M.; Behnamfar, F.; Vafaeian, M. A semi-analytical model for estimating seismic behavior of buried steel pipes at bend point under propagating waves. *Bull. Earthq. Eng.* **2013**, *11*, 1373–1402. [CrossRef]
29. Sun, M.; Chen, Y.; Zhao, H.; Li, X. Analysis of the impact factor of burst capacity models for defect-free pipelines. *Int. J. Pres. Ves. Pip.* **2022**, *200*, 104805. [CrossRef]
30. Sun, M.; Zhao, H.; Li, X.; Liu, J.; Xu, Z. New evaluation method of failure pressure of steel pipeline with irregular-shaped defect. *Appl. Ocean Res.* **2021**, *110*, 102601. [CrossRef]
31. Sun, M.; Fang, H.; Wang, N.; Du, X.; Zhao, H.; Zhai, K. Limit state equation and failure pressure prediction model of pipeline with complex loading. *Nat. Commun.* **2024**, *15*, 4473. [CrossRef]
32. American Lifelines Alliance. *Guidelines for the Design of Buried Steel Pipe*; ASCE: Reston, VA, USA, 2001.
33. Deshpande, V.S.; Fleck, N.A. Isotropic constitutive models for metallic foams. *J. Mech. Phys. Solids* **2000**, *48*, 1253–1283. [CrossRef]
34. Wang, Y.; Pokharel, R.; Lu, J.; Zhai, X. Experimental, numerical, and analytical studies on polyurethane foam-filled energy absorption connectors under quasi-static loading. *Thin Wall. Struct.* **2019**, *144*, 106257. [CrossRef]
35. Gao, X.; Shao, Y.; Xie, L.; Yang, D. Behavior of API 5L X56 submarine pipes under transverse impact. *Ocean Eng.* **2020**, *206*, 107337. [CrossRef]
36. Taherkhani, A.; Sadighi, M.; Vanini, A.S.; Mahmoudabadi, M.Z. An experimental study of high-velocity impact on elastic–plastic crushable polyurethane foams. *Aerosp. Sci. Technol.* **2016**, *50*, 245–255. [CrossRef]
37. Zarei, H.R.; Ghamarian, A. Experimental and numerical crashworthiness investigation of empty and foam-filled thin-walled tubes with shallow spherical caps. *Exp. Mech.* **2014**, *54*, 115–126. [CrossRef]


**Disclaimer/Publisher's Note:** The statements, opinions and data contained in all publications are solely those of the individual author(s) and contributor(s) and not of MDPI and/or the editor(s). MDPI and/or the editor(s) disclaim responsibility for any injury to people or property resulting from any ideas, methods, instructions or products referred to in the content.